iScience

Article

Volume electron microscopy reveals 3D synaptic nanoarchitecture in postmortem human prefrontal cortex

Graphical abstract

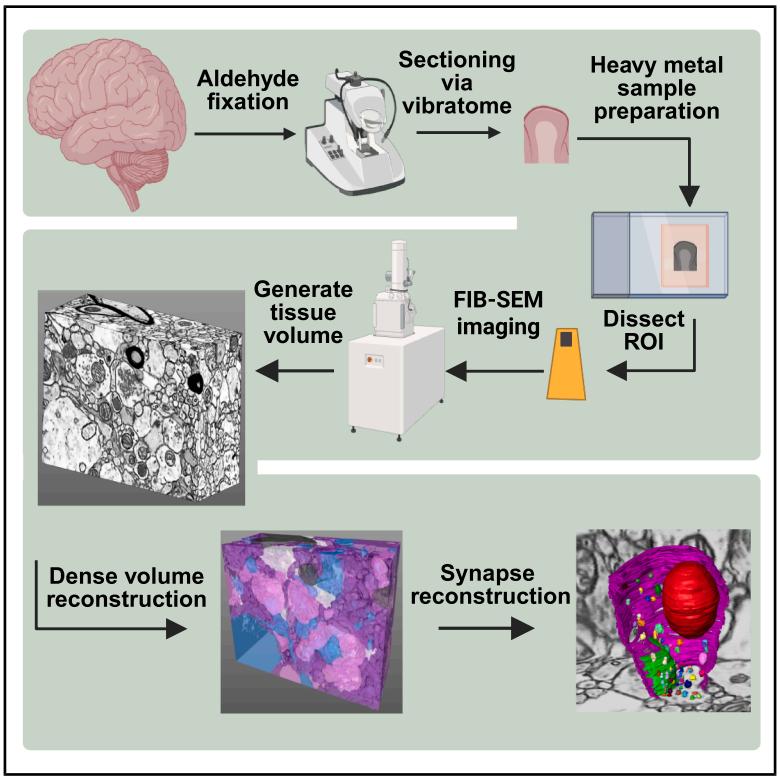

Authors

Jill R. Glausier, Matthew Maier, Cedric Bouchet-Marquis, ..., Jiying Ning, David A. Lewis, Zachary Freyberg

Correspondence

glausierjr@upmc.edu

In brief

Neuroscience

Highlights

- Human brain tissue obtained postmortem is suitable for 3D electron microscopy
- Postmortem processes did not affect fundamental synaptic relationships
- Ultrastructural correlates of *in vivo* synaptic function are preserved postmortem
- 3D EM analysis offers a way to infer functioning of individual synapses in human brain

Glausier et al., 2025, iScience *28*, 112747
July 18, 2025
https://doi.org/10.1016/j.isci.2025.112747

CellPress

iScience

CellPress
OPEN ACCESS

Article

Volume electron microscopy reveals 3D synaptic nanoarchitecture in postmortem human prefrontal cortex

Jill R. Glausier,[1,6,*] Matthew Maier,[1] Cedric Bouchet-Marquis,[2] Ken Wu,[2] Tabitha Banks-Tibbs,[1,3,4] Darlene Melchitzky,[1] Jiying Ning,[1] David A. Lewis,[1] and Zachary Freyberg[1,5]

[1]Department of Psychiatry, University of Pittsburgh, Pittsburgh, PA, USA
[2]Materials and Structural Analysis, Thermo Fisher Scientific, Hillsboro, OR, USA
[3]Department of Human Genetics, University of Pittsburgh, Pittsburgh, PA, USA
[4]College of Medicine, The Ohio State University, Columbus, OH, USA
[5]Department of Cell Biology, University of Pittsburgh, Pittsburgh, PA, USA
[6]Lead contact
*Correspondence: glausierjr@upmc.edu
https://doi.org/10.1016/j.isci.2025.112747

SUMMARY

Synaptic function is reflected in quantifiable ultrastructural features using electron microscopy (EM) approaches. This coupling of synaptic function and ultrastructure suggests that *in vivo* synaptic function can be inferred from EM analysis of *ex vivo* human brain tissue. To investigate this, we employed focused ion beam-scanning electron microscopy (FIB-SEM), a volume EM (VEM) approach, to generate ultrafine-resolution, three-dimensional (3D) micrographic datasets of postmortem human dorsolateral prefrontal cortex (DLPFC), a region with cytoarchitectonic characteristics distinct to human brain. Synaptic, sub-synaptic, and organelle measures were highly consistent with findings from experimental models that are free from antemortem or postmortem effects. Further, 3D neuropil reconstruction revealed a unique spiny dendritic shaft that exhibited several ultrastructural features characteristic of neuronal segments engaged in synaptic plasticity. Altogether, our findings provide critical proof-of-concept data demonstrating that *ex vivo* VEM analysis appears as an effective approach to infer *in vivo* synaptic functioning in human brain.

INTRODUCTION

Coordinated, adaptable synaptic signaling underlies core brain processes such as thought, emotion, learning, and memory.[1] Loss or dysfunction of synaptic signaling is proposed as the pathophysiological substrate for severe brain disorders including schizophrenia[2,3] and autism spectrum disorder,[4] which are characterized by impairments to these core brain processes. Thus, investigating synaptic signaling in the human brain is critical to advance the understanding of both normal synaptic function and the nature of synaptic dysfunction in disease.

The morphological substrate of synaptic communication is the synaptic complex,[5,6] comprised in its most elemental form by a presynaptic axonal bouton apposed to a postsynaptic element, such as a dendritic spine. The synaptic complex and its constituent components can be directly visualized in human brain tissue with electron microscopy (EM) approaches. A substantial literature in experimental, non-human model organisms demonstrates that *in vivo* synaptic function is directly reflected in ultrastructural measures obtained *ex vivo* via EM, and this is especially evident in the glutamate synaptic system. For example, presynaptic active zone size reflects the relative level of axonal bouton activation and glutamate release probability.[7–11] Postsynaptic density (PSD) size is strongly correlated with excitatory postsynaptic potential amplitude[7] and abundance of AMPA receptors.[12–16] Because synaptic communication represents the largest energy-demanding process in the brain,[17–26] relative ATP consumption at synaptic units is reflected by the abundance,[25,27,28] size,[27,29] and morphology[30–33] of mitochondria. Moreover, a fundamental feature of synaptic communication is that pre- and postsynaptic elements act together as a functional unit,[34,35] and EM ultrastructural measures also capture this core aspect of synaptic functioning.[36] For example, presynaptic glutamate release probability and presynaptic active zone size correlate with PSD size.[7,8] Likewise, presynaptic mitochondrial abundance is related to PSD size.[33,37] This wealth of data from experimental models demonstrates that *in vivo* synaptic function can be derived from quantitative EM analysis of *ex vivo* preserved brain tissue. However, whether these synaptic function-ultrastructure relationships are present in human brain is unclear.

Human brain tissue is sourced either from biopsies obtained during neurosurgical interventions or from donations obtained postmortem. However, postmortem donations are the exclusive source for brain tissue from individuals unaffected by brain disorders during life and for individuals with neuropsychiatric disorders like schizophrenia, autism spectrum disorder, or

Alzheimer's disease, which are currently not diagnosed or treated via neurosurgery. Because whole brains are typically obtained, postmortem sources also permit analysis of multiple brain regions from a single subject, as well as analysis of regions not typically obtained during neurosurgery. For example, the dorsolateral prefrontal cortex (DLPFC) is a higher-order, multimodal association area[38,39] that is uniquely expanded in humans[40,41] and is considered a key site of synaptic dysfunction in human-specific psychiatric disorders.[42–45] EM analysis of postmortem DLPFC tissue presents a unique opportunity to investigate synaptic and sub-synaptic morphological impairments present in individuals with psychiatric disorders relative to individuals unaffected by brain disorders.

Although EM studies of postmortem human DLPFC have been published (for examples, see[46–49]), this earlier work utilized a conventional two-dimensional (2D) approach to study single ultrathin (~60 nm) sections in order to generate estimates of three-dimensional (3D) features. Furthermore, a Z resolution of ~60 nm may obscure critical ultra- and nanostructures, even when ultrathin sections are studied in series. The potential confounding effects of postmortem biological processes and of tissue storage on tissue fidelity, particularly at the ultrastructural level of resolution, remain a concern. To address these EM methodological limitations and postmortem tissue concerns, the primary goal of this study was to determine how well 3D synaptic nanoarchitecture and relationships are maintained in postmortem human brain, within the context of the surrounding neuropil,[50] using a tissue preservation and storage approach compatible with EM analyses.

We performed a 3D quantitative analysis of glutamate synaptic complexes in postmortem human DLPFC via focused ion beam-scanning electron microscopy (FIB-SEM) with tissue samples previously stored for ~8 years. FIB-SEM is a volume electron microscopy (VEM) approach that works by using a focused ion beam to remove a pre-defined thickness of tissue, followed by imaging of the newly exposed cross-section face via SEM in a sequential manner until the entire tissue block is imaged.[51] By iterating through these steps, a 3D volume of brain tissue is acquired with ultrafine Z resolution. Using this innovative technology, we imaged and densely reconstructed a 3D volume of DLPFC with essentially no loss of information at a 5 nm milling step-size from an individual with no brain disorders present during life. Taking advantage of the rich data within this 3D brain volume, we completed targeted, 3D reconstructions and volumetric analyses of 50 Type 1 axo-spinous glutamatergic synapses. Quantitative analyses revealed that the fundamental relationships between pre- and postsynaptic components identified in non-human experimental systems, which are not associated with any postmortem biological processes, is clearly evident in postmortem human brain tissue. Furthermore, dense reconstruction of DLPFC neuropil revealed a unique pyramidal neuron dendritic segment exhibiting features and structures that indicate a large reserve of molecular and morphological resources to maintain synaptic communication. Overall, our findings provide a critical proof-of-concept that *ex vivo* VEM analysis offers a valuable and informative means to infer key aspects of *in vivo* functioning of individual synaptic complexes in human brain.

RESULTS

Long-term preservation and neuroanatomical-guided sampling of postmortem human brain tissue for FIB-SEM imaging

The current approach was designed to preserve the gross and microscopic anatomical features of brain tissue to permit sampling of specific cortical regions, layers, and sub-layers for ultrastructural analyses (detailed in STAR Methods). Briefly, the middle frontal gyrus, a primary component of the human DLPFC, was identified based on gyral and sulcal features (Figure 1A). A tissue sample containing cortical layers 1–6 and the underlying white matter was dissected (Figure 1B), immersion-fixed in 4% paraformaldehyde/0.2% glutaraldehyde for 48 h, and then sectioned at 50-μm intervals. Tissue sections were stored in a cryoprotectant solution (30% ethylene glycol/30% glycerol) at −30°C for ~8 years.

Stored sample integrity was first evaluated at the light microscopic level. Nissl stain revealed that the canonical laminar structure of DLPFC, as well as neuronal and glial cell morphology, were preserved (Figure 1C). An adjacent section underwent EM sample preparation using an approach developed by Hua et al.[52] that was modified to optimize preservation, staining and contrast of postmortem human brain tissue sections from long-term storage (modifications detailed in STAR Methods). These modifications preserved the benefits of the Hua et al.[52] approach, which was developed to stain larger volumes of cortex harvested from mice after transcardial perfusion.[52] Tissue with a staining intensity of sufficiently high contrast to visualize neuropil components via FIB-SEM and maintained staining intensity throughout the depth of the tissue section was achieved with these modifications (Figures 1D, 1E, and 2).

Qualitative assessment of VEM-imaged DLPFC layer 3 neuropil volume

Qualitative evaluation of the 3D VEM dataset of postmortem human DLPFC layer 3 revealed excellent ultrastructural preservation[48] (Figures 2 and 3; Videos S1 and S2). Cellular and organelle plasma membranes were intact, and these structures had a paucity of swelling, deformation, or other signs of autolysis. All expected components of cortical neuropil were identified, including (1) spiny dendritic shafts, which exclusively emanate from local glutamatergic pyramidal neurons, (2) axonal boutons forming Type 1 synapses predominately from local or associational glutamatergic neurons, (3) aspiny dendritic shafts which exclusively emanate from local inhibitory interneurons, (4) axonal boutons forming Type 2 synapses almost exclusively from local inhibitory interneurons, and (5) glial processes from local astrocytes (Figures 2, 3, and 4). Type 1 and Type 2 synaptic complexes and sub-synaptic structures were also readily detected in the 3D neuropil volume (Figures 3 and 4). Consistent with the cytoarchitectonic characteristics of DLPFC layer 3, nearly all axonal processes were unmyelinated, likely reflecting glutamatergic pyramidal neuron intrinsic or associational collaterals.[53–55] Pyramidal neuron dendritic spines were typically the recipient of Type 1 synapses, and these spines often contained a spine apparatus or smooth endoplasmic reticulum (SER; Figures 3A, 3B, 3E, and 4). As expected, mitochondria were

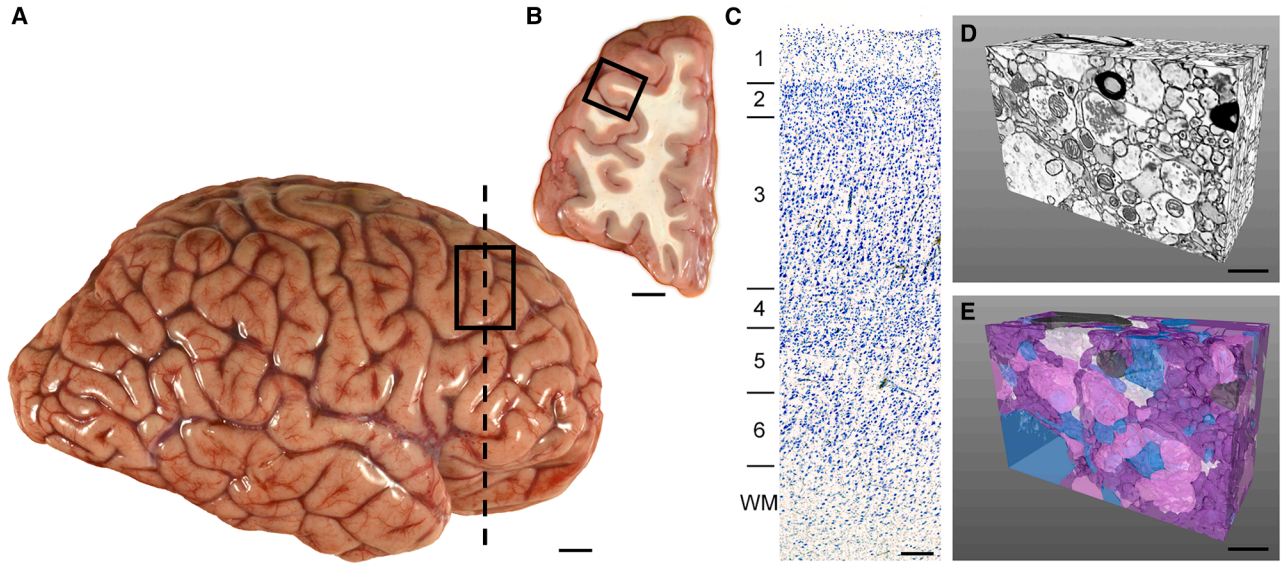

Figure 1. Overview of postmortem human brain tissue sampling and 3D reconstruction

(A) Lateral view of a representative postmortem human brain hemisphere before fixation. Rectangle shows the approximate location of the DLPFC region.

(B) Coronal view of the DLPFC at the approximate rostro-caudal level indicated by the vertical dashed line in (A). Box indicates the approximate region sampled for this study.

(C) Nissl-stained tissue section from the approximate location shown by the box in B. Cortical layers are numbered, and layer 3 from an adjacent tissue section was sampled for the current study.

(D) Postmortem human DLPFC layer 3 neuropil volume imaged in 3D via FIB-SEM and analyzed in the current study.

(E) Corresponding dense 3D reconstruction of neuronal and glial profiles shown in (D). Glutamate axonal boutons (pink), dendritic shafts and spines (blue), unmyelinated axons (purple), myelinated axons (dark gray), and astrocytic processes (white). Scale bar in A is 2 cm, B is 1 cm, C is 0.5 mm, and D and E are 1 μm.

not observed in spine heads, but were observed in the parent dendritic shaft near the base of the spine neck (Figure 3B) or near Type 1 synapses that formed onto dendritic shafts (Figure 3C). Type 2 synapses, presumably GABAergic, were identified on neuronal somata (Figure 3D). We also observed dually innervated spines receiving a Type 1 and a Type 2 synapse (Figures 3E and 3F).

Mitochondria exhibited ultrastructural features characteristic of preserved integrity, including intact outer and inner membranes, organized cristae, homogeneous matrix, and an absence of swollen, deformed, or fragmented morphologies (Figures 2 and 3). Mitochondria exclusively exhibited a globular or elongated morphology, further consistent with a lack of deleterious postmortem biological processes.[30,48,56] Consistent with the association of distinct mitochondrial morphologies with high or low energy states,[30] we show examples of a globular mitochondrion, which is associated with greater mitochondrial energy production, in an axon bouton forming a synapse (Figures 5A–5C), and an elongated mitochondrion, associated with lower energy production, within an axon bouton lacking a synapse (Figures 5D–5F). Reconstructed cristae in the globular mitochondrion are large, spanning much of the mitochondrial volume, whereas the cristae in the elongated mitochondrion appear more truncated. The calculated cristae:matrix volume ratio is 0.7 for the globular mitochondrion and 0.4 for the elongated mitochondrion, consistent with prior findings that mitochondrial cristae:matrix volume ratios are smaller at less active boutons.[33]

In qualitatively evaluating the complete 3D volume, we noted a pyramidal neuron dendritic shaft with several distinctive ultrastructural features (Figures 6, 7, and S1). Unlike nearby dendrites that exhibited a relatively electron-lucent cytoplasm (a typical feature of dendrites[57]), this dendrite exhibited an electron-dense cytoplasm (Figures 7A–7F), indicating an abundance of macromolecules such as proteins and lipids.[58] The dendrite also appeared to contain distinct sub-cellular structures situated within the cytoplasm, as if piercing through the shaft (Figures 6B and 6C). The dendrite and these invaginated structures were reconstructed in 3D to better interrogate their sub-cellular and synaptic features and relationships.

The pyramidal neuron dendrite spanned all 1,580 ortho-slices, for a length of 7.9 μm in the Z dimension and a total volume of 2.0 mm^3, inclusive of spines (Figure 6). The dendritic shaft and protruding spines received a total of eight synapses: six were Type 1 and two were Type 2 (presumptive GABAergic) synapses. Each spine received a Type 1 glutamatergic synapse and one spine was dually innervated by a Type 1 and a Type 2 synapse (Figure 6D). Additionally, the parent shaft directly received two Type 1 synapses and one Type 2 synapse (Figure 6D). Thus, this dendritic shaft exhibits multiple synaptic features consistent with greater neurotransmission. For example, dually innervated cortical pyramidal neuron spines represent sites with greater synaptic gating and integration relative to spines receiving a single Type 1 synaptic input,[60] and Type 1 synapses are infrequently formed directly onto the shaft of spiny dendrites, though two are formed here.[61]

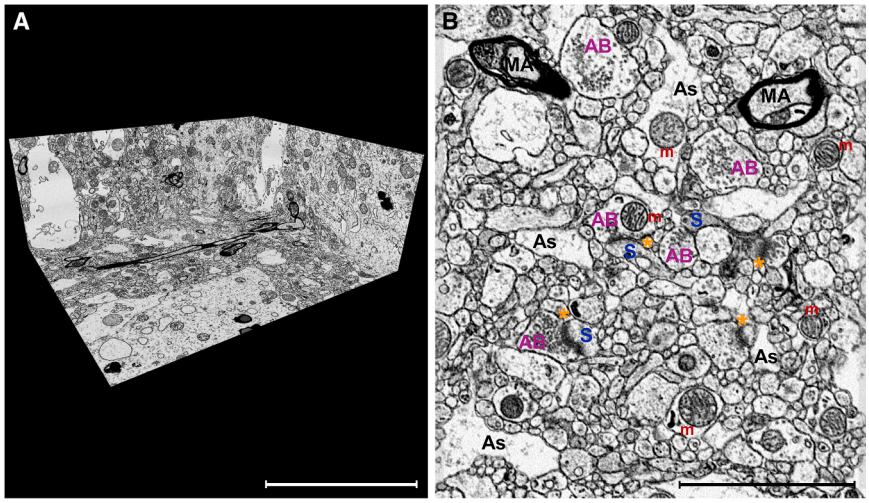

Figure 2. Excellent ultrastructural preservation of postmortem human brain tissue processed for FIB-SEM imaging

(A) A perspective overview of a volume of DLPFC layer 3 captured with an isotropic voxel size of 5 × 5 × 5 nm.

(B) A representative SEM image illustrating excellent preservation of the neuropil. Select glutamate synapses labeled: axonal bouton (AB) directly apposed to a dendritic spine (S) containing an electron-dense PSD (asterisk). Additional neuropil components, such as astrocyte processes (As), myelinated axons (MA), and mitochondria (m) are also labeled. Scale bar is 10 μm in A and 3 μm in (B).

Four distinct cylindrical structures coursing through the cytoplasm of the dendritic shaft were revealed by 3D reconstruction. The plasma membranes of these invaginated structures were clearly differentiated from the plasma membrane surrounding the dendritic cytoplasm and, unexpectedly, they did not connect to any parent structure (Figures 6B, 6C, 7, and S1). On average, the invaginated structures spanned 1.7 ± 0.55 μm in the Z dimension, had a diameter of 295.4 ± 77.0 nm and volume of 0.12 ± 0.68 μm^3. The size, ultrastructural appearance, and absence of a connecting parent structure is highly consistent with dendritic and axonal filopodia.[62,63] The filopodia-like structures were not uniformly distributed throughout the dendritic shaft, but instead were clustered within the dendritic segment directly receiving Type 1 and Type 2 synapses and at the base of spines 1 and 2 (Figures 6D, 7, and S1). Additional distinctive ultrastructural features were present, including abundant organelles such as mitochondria, SER, and putative endosomes (Figures 7 and S1). Altogether, these observations describe a distinctive pyramidal neuron dendritic segment that has a uniquely large reserve and repertoire of molecular and morphological resources to maintain postsynaptic responses to glutamatergic and GABAergic inputs.

Qualitative evaluation of the complete 3D volume showed that invaginated filopodia-like structures were occasionally observed in other dendritic shafts. Interestingly, these dendrites exhibited many features typical of dendritic shafts: electron-lucent cytoplasm, synapses rarely formed onto the shaft, and a relative paucity of SER and endosomes (Figure S2). These findings indicate that invaginated filopodia-like structures are not exclusive to neuronal areas with a high resource demand, and may represent one of the diverse mechanisms that can deliver resources to distal neuronal processes.

Quantitative analysis of densely reconstructed DLPFC layer 3 neuropil sub-volume

Dense reconstruction of the sub-volume revealed the respective contributions of each type of neuronal and glial process (Table 1). Synaptic analysis showed greater density of Type 1 synapses compared to Type 2 synapses, with an overall synaptic density of 0.39/μm^3. Axonal boutons forming Type 1 synapses preferentially targeted dendritic spines over shafts (Table 2). Analysis of all 28 axonal boutons identified in the sub-volume revealed that 71% (n = 20) formed a Type 1 synapse, 18% (n = 5) formed a Type 2 synapse, and 11% (n = 3) did not form an identifiable synapse. This finding is consistent with prior studies showing that ~10% of boutons may be non-synaptic at any given point in time.[64,65]

Quantitative analysis of synaptic features in a layer 3 neuropil sub-volume imaged at lower resolution

Substantially larger volumes of tissue can be generated by imaging at a lower resolution, and multiple studies have shown that some synaptic measures are suitable for analysis at resolutions lower than 5 nm^3 voxel size (for example, see Schmidt et al.[66]). To determine whether synaptic features can be reliably measured in neuropil imaged via FIB-SEM at a lower resolution, we analyzed a DLPFC layer 3 neuropil volume obtained using a slice thickness and pixel size four times greater than the primary volume, 20 × 20 × 20 nm, generating a final volume ~25% larger (270 μm^3) than the high-resolution volume (Figure S3; Video S3).

Synaptic analysis showed greater density of Type 1 synapses compared to Type 2 synapses, with an overall synaptic density of 0.39/μm^3, identical to that identified in the high-resolution volume. Axonal boutons forming Type 1 synapses preferentially targeted dendritic spines over shafts (Table 2). Analysis of all 115 axonal boutons identified in the sub-volume revealed that 82% (n = 94) formed a Type 1 synapse, 9.5% (n = 11) formed a Type 2 synapse, and 8.5% (n = 10) did not form an identifiable synapse, consistent with the high-resolution findings. However, the ability to definitively identify the neuronal compartment postsynaptic to Type 1 synapses was impaired at lower resolution (Table 2). For example, at high resolution 70% of Type 1 synapses were identified onto spines and 30% onto shafts, whereas at low resolution 48% of Type 1 synapses were identified onto spines, 35% onto shafts, and 17% onto non-identifiable elements (Table 2). Altogether, these results support the idea that identification of axonal boutons and Type 1 and Type 2 synapses is equally as reliable in volumes imaged at 5 nm^3 and 20 nm^3 voxel sizes, but that postsynaptic target identification may be affected.

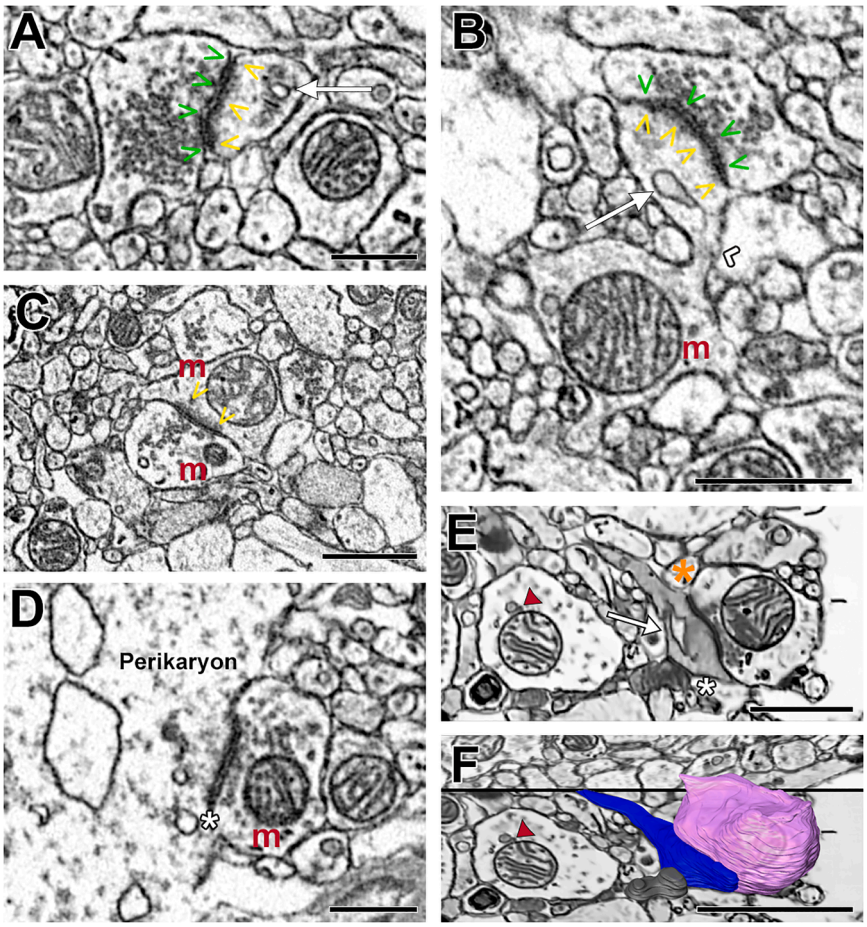

Figure 3. Representative images illustrating Type 1 and Type 2 synapses identified in postmortem human DLPFC layer 3

(A) Axonal bouton filled with synaptic vesicles and forming a Type 1 synapse onto a dendritic spine containing a spine apparatus.

(B) A parent dendritic shaft containing a mitochondrion positioned at the base of the spine neck. The spine head contains SER and is receiving a Type 1 synapse.

(C) A bouton forming a Type 1 synapse onto a dendritic shaft containing a mitochondrion.

(D) Neuronal cell body receiving a Type 2, presumably GABAergic, synapse.

(E) A dendritic spine with SER and electron-dense cytoplasm receiving a Type 1 and a Type 2 synapse. In an adjacent dendritic shaft, the mitochondrion is tethered to an electron dense vesicle.

(F) 3D reconstruction of the Type 1 bouton (pink), dendritic spine (blue) and the Type 2 bouton (gray) shown in (E) within the context of the surrounding neuropil. Symbol legend: green arrowheads- active zone; yellow arrowheads- PSD; white arrow-spine apparatus or SER; white chevron-spine neck; orange asterisk- Type 1 synapse; white asterisk- Type 2 synapse; red arrowhead-mitochondrial-tethered vesicle. Scale bar is 1.5 μm in (A, B, D and F); and is 1 μm in (E).

Targeted quantitative analysis of type 1 synaptic, sub-synaptic, and organelle structures

To further interrogate synaptic features of postmortem human DLPFC, we next completed a targeted analysis of the predominant synaptic population, Type 1 glutamatergic axo-spinous synapses, at high resolution. A total of 50 Type 1 glutamatergic axo-spinous synapses were systematically randomly identified and reconstructed in 3D. Quantitative analysis (Figure 8) revealed the average sizes of synaptic axonal boutons (0.46 ± 0.26 μm^3), synaptic spines (0.15 ± 0.13 μm^3), presynaptic active zones (5.5 ± 3.8e^6 nm^3), and PSDs (8.0 ± 5.1e^6 nm^3). A large variability in the sizes of sub-synaptic components were reflected in these quantitative measures. Variability in the sizes of synaptic components likely reflects the dynamic range of synaptic activity and plasticity contributing to complex neural computation,[67–69] which is a defining functional feature of the human DLPFC.[38,70] Reconstructions of the smallest and largest structures (Figure S4) illustrate this synaptic diversity.

Mitochondria, identified in 52% (n = 26/50) of Type 1 synaptic boutons, had an average volume of 0.09 ± 0.05 μm^3. All bouton mitochondria exhibited globular morphology (mean aspect ratio = 0.99). Of the synaptic spines, 88% (n = 44/50) contained a spine apparatus or SER. Because these core synaptic components were sufficiently preserved for quantitative volumetric and morphologic analysis, we next sought to determine whether the within- and *trans*-synaptic structure relationships that reflect functional synaptic communication were maintained postmortem.

Targeted quantitative analysis of Type 1 pre- and postsynaptic structure relationships

Presynaptic bouton and active zone volumes were positively correlated (r = 0.60, p = 4.0e^{-6}; Figure 9A), as were spine and PSD volumes (r = 0.43, p = 0.002; Figure 9B). Analyses of *trans*-synaptic structures revealed positive correlations between presynaptic bouton and postsynaptic spine volumes (r = 0.37, p = 0.008; Figure 9C) and presynaptic active zone and PSD volumes (r = 0.76, p = 1.2e^{-10}; Figure 9D). To further evaluate whether trans-synaptic ultrastructural relationships persist in the postmortem human brain, we compared synapses based on the presence of mitochondria, or a spine apparatus or SER, organelles indicative of greater synaptic function and activity.[28,29,71,72] Type 1 axo-spinous synapses with presynaptic mitochondria had significantly greater bouton, active zone, and PSD volumes, and were significantly more likely to target a spine with a spine apparatus or SER (Table 3). Type 1 axo-spinous synapses with a postsynaptic spine apparatus or SER had significantly greater mean spine, active zone, and PSD volumes (Table 4). These convergent results support our interpretation

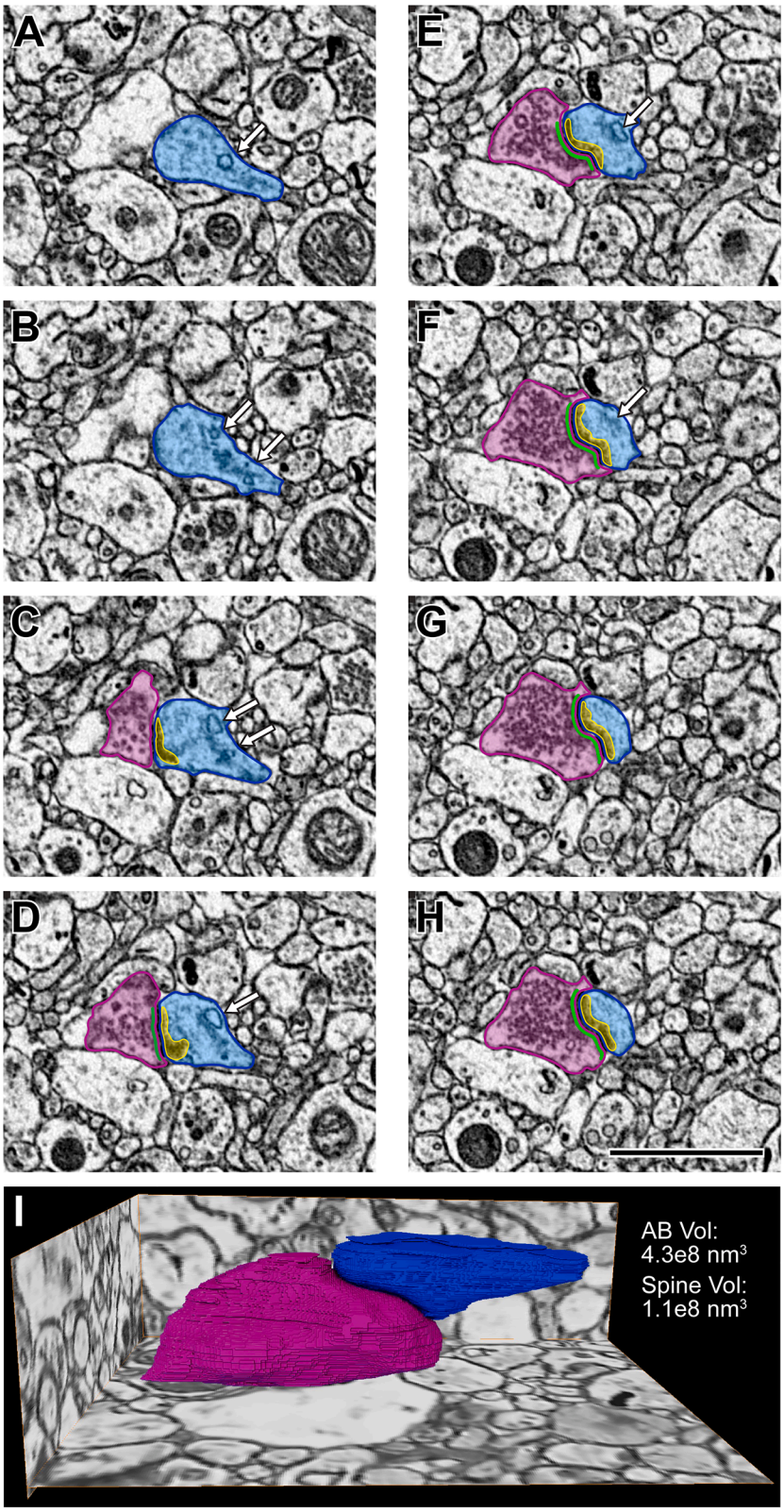

Figure 4. A series of electron micrographs viewed in the XY coordinate plane and the completed volume reconstructions of a Type 1 glutamatergic synapse in postmortem human DLPFC layer 3

(A–H) Each panel represents 5 nm increments milled by the gallium FIB. In (A) and (B) the dendritic spine (blue) is identified. (C) is the initial visualization of the glutamatergic synaptic structure including a presynaptic axonal bouton (pink) with an active zone (green) and a postsynaptic spine (blue) containing a PSD (yellow). Note the presence of a spine apparatus (white arrow) in (A–F). Scale bar is 2 μm.

(I) Glutamatergic synaptic structure reconstructed in 3D shown in the context of the surrounding tissue. Volume measurements for the axonal bouton (pink) and the spine (blue) are provided.

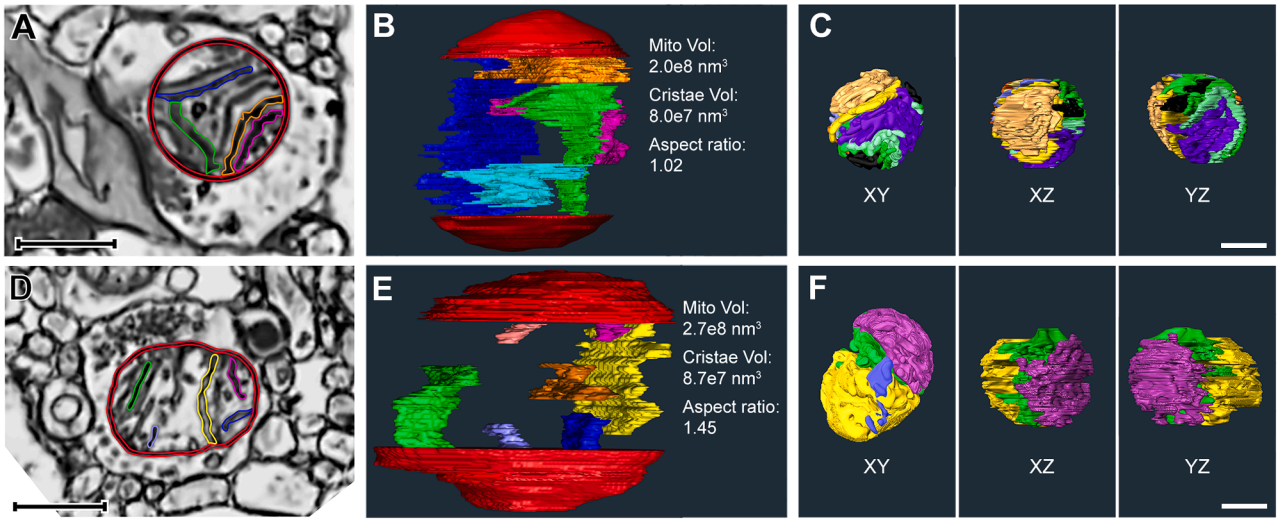

Figure 5. Mitochondria in postmortem human DLPFC layer 3

(A–C) Globular mitochondrion; (D–F) Elongated mitochondrion. (A) A 2D image of a globular mitochondrion in an axonal bouton forming a Type 1 synapse. Inner and outer mitochondrial membranes shown in red, and a subset of cristae are segmented using multiple colors. (B) Internal view of the 3D reconstructed globular mitochondrion and cristae. In order to optimize visualization in a 2D image, only a subset of cristae volume reconstructions are shown, and inner and outer mitochondrial membranes are partially reconstructed. Total mitochondrion and cristae volumes are provided. The aspect ratio is characteristic of globular morphology. (C) 3D reconstructions of all cristae within the globular mitochondrion shown in the XY, XZ, and YZ dimensional planes. (D) A 2D image of an elongated mitochondrion in a non-synaptic axonal bouton. (E) Internal view of the 3D reconstructed elongated mitochondrion and cristae. In order to optimize visualization in a 2D image, only a subset of cristae volume reconstructions are shown, and inner and outer mitochondrial membranes are partially reconstructed. Total mitochondrion and cristae volumes are provided. The aspect ratio is characteristic of elongated morphology. (F) 3D reconstructions of all cristae within the elongated mitochondrion shown in the XY, XZ, and YZ dimensional planes. Scale bar in (A) is 500 nm, (C and F) is 300 nm, (D) is 555 nm.

that the fundamental ultrastructural features reflecting synaptic function and activity previously observed in brains of model organisms are similarly preserved in postmortem human DLPFC.

DISCUSSION

We employed an advanced VEM imaging approach, FIB-SEM, to determine if 3D ultrastructural correlates of *in vivo* glutamate synapse function and activity are preserved *ex vivo* in the postmortem human brain. To address this, we first modified an existing workflow[52] to generate postmortem human DLPFC tissue samples with optimal ultrastructural preservation and enhanced-contrast staining required for FIB-SEM imaging. Second, we successfully imaged a volume (2,630 μm^3) of human DLPFC layer 3 with a 5 nm isotropic voxel resolution via FIB-SEM, ensuring little to no loss of information and equivalent resolution in all dimension planes, and a comparative second volume imaged with a 20 nm isotropic voxel size. Third, we implemented a semi-automated data collection approach to complete a dense 3D reconstruction of the high-resolution sub-volume of postmortem human DLPFC layer 3. Finally, we reconstructed sub-cellular, sub-synaptic, and mitochondrial components within 50 glutamate axo-spinous synapses that were systematically randomly selected. Quantitative analysis of these 3D datasets revealed that ultrastructural features which reflect synaptic function and activity were preserved within and across individual synapses in postmortem human brain tissue stored for ~8 years before EM sample preparation. Thus, our findings provide proof-of-concept that established ultrastructural indices of *in vivo* functioning of individual synapses can be quantitatively investigated *ex vivo* in human brain tissue obtained postmortem and analyzed by FIB-SEM.

DLPFC layer 3 neuropil organization was revealed by dense reconstruction and quantitative analysis. The relative proportion of DLPFC layer 3 neuropil occupied by each type of cellular compartment was remarkably similar to recent VEM findings in samples of temporal cortex layer 3 that were obtained by biopsy,[73] as was the volumetric proportion reflecting extracellular space in biopsy-obtained prefrontal cortex.[74] The mean synaptic density observed by VEM imaging of biopsy cortical samples[73,75–79] ranges from 0.0002/μm^3 to 0.74/μm^3, and of autopsy cortical samples[75,80–85] from 0.40/μm^3 to 0.76/μm^3. Our current finding of 0.39/μm^3 in DLPFC layer 3 is consistent with these existing data, which span multiple cortical areas and layers, and is also consistent with previous findings in monkey DLPFC layer 3.[86]

We identified that 80% of DLPFC layer 3 synapses were Type 1 and the remaining 20% were Type 2. These proportions are highly consistent with findings in layer 3 of biopsied temporal cortex,[73] but lower than the findings of 92–95% Type 1 synapses in postmortem temporal cortex layers 2–5,[75,81–85] anterior cingulate cortex layer 3,[80] and layer 3 of primary visual, motor and somatosensory cortices.[80] Findings regarding the effects of postmortem interval (PMI) on Type 1 and 2 synapse identification are highly mixed [for review see Krassner e al.[87]]. Some evidence suggests that PSD size may increase with PMI,[88] resulting in the possible mis-identification of Type 2 synapses as Type 1. However, our findings indicate this potential confound was likely not

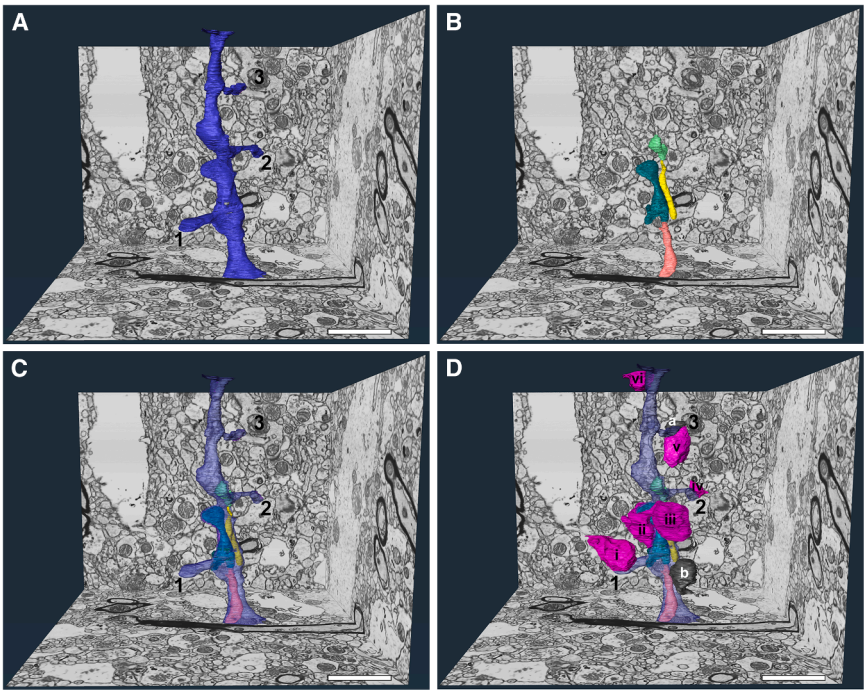

Figure 6. 3D reconstructions of a complex dendritic shaft with filopodia-like structures coursing through the dendritic cytoplasm

(A) A perspective overview of a volume of DLPFC layer 3 with a dendritic shaft completely reconstructed (blue). Multiple spines (numbered 1–3) protrude from the parent shaft, and a partial fourth spine is visible at the top of the volume for a mean spine occurrence of 0.5/μm.

(B and C) Similar perspective overviews illustrating the four filopodia-like structures (salmon, teal, yellow and lime green) completely enveloped within the cytoplasm of the dendritic shaft. The yellow, teal and lime green reconstructions are fully contained within the tissue volume and are not connected to any surrounding structure. The entirety of the salmon reconstruction is not present in the total volume.

(D) The dendritic shaft and protruding spines received a total of eight synapses: six Type 1 synapses from glutamatergic boutons (pink, labeled i-vi) and two Type 2 synapses from presumably GABAergic boutons (gray, labeled a and b). Spines 1 and 2 each received a single synapse from distinct glutamatergic boutons (i and iv, respectively). Spine 3 was dually innervated by a glutamatergic and a presumably GABAergic bouton (v and a, respectively). The partial spine (top) received at least one synapse from a glutamatergic bouton (vi). Scale bars are 2 μm.

present, and/or the rich, isotropic, 3D ultrastructural data available for every synaptic contact mitigated any potential PMI effect on synapse identification. Finally, although our findings in the high- and low-resolution volumes regarding the postsynaptic targets of Type 1 synapses differed, all findings are within the range of existing studies. For example, previous VEM studies of biopsy[76,78,79] and autopsy[75,80–83] cortical samples found that 82–90% and 55–73% of Type 1 synapses were formed onto dendritic spines, respectively. Thus, all neuropil components, including Type 1 and Type 2 synapses, were identifiable and quantifiable via FIB-SEM imaging at multiple resolutions using the tissue processing workflow optimized for postmortem human brain.

Targeted 3D ultrastructural analysis of Type 1 axo-spinous glutamatergic synapses similarly demonstrated that synaptic nanoarchitecture is preserved in postmortem human DLPFC. For example, in model systems, active zone and PSD sizes are highly correlated, and this finding reflects that pre- and postsynaptic components must act together as a functional unit for effective synaptic communication.[34,35] Active zone and PSD sizes are also diverse in the normal brain, which reflects the dynamic range of synaptic activity and plasticity contributing to complex neural computation.[67–69] Both of these core synaptic features were clearly evident in postmortem human DLPFC, qualitatively and quantitatively, suggesting that not only did the synaptic functional unit remain intact postmortem, but the expected diversity of synaptic component sizes was also preserved.

Analysis of mitochondria and spine apparatuses or SER, synaptic organelles whose presence is indicative of greater activity and neurotransmission,[29,72] further demonstrated preserved glutamatergic synaptic relationships within postmortem DLPFC. For example, mitochondria are trafficked to more active synaptic boutons, providing the required energetic support for efficient neurotransmitter release.[89,90] Similarly, spine apparatuses and SER are present in dendritic spines that are more synaptically active, enhancing postsynaptic Ca^{2+} buffering and post-translational modification capabilities.[71,72] Consistent with these findings from model organisms, and a study using serial section EM analysis of postmortem human hippocampus,[33] Type 1 axo-spinous synapses with presynaptic mitochondria had significantly greater mean active zone and PSD volumes, and significantly more of these synapses contained a spine apparatus. Likewise, glutamatergic synapses with a postsynaptic spine apparatus or SER exhibited significantly greater mean active zone and PSD volumes, and significantly more of these synapses contained presynaptic mitochondria. Together, the synaptic nanoarchitecture and organelle findings provide convergent support that indices of *in vivo* synaptic function and activity can be interrogated *ex vivo* in postmortem human brain tissue via quantitative FIB-SEM imaging and analysis.

In the DLPFC layer 3 neuropil volume, we reconstructed a pyramidal neuron dendritic shaft that spanned all 1,580 ortho-slices. Notably, this shaft exhibited unique and complex ultrastructural features that are experimentally shown to be characteristic of heightened synaptic signaling and plasticity. Unlike nearby shafts, which exhibited ultrastructure features typical of dendrites in the cortical neuropil (e.g., electron-lucent cytoplasm),[57] this dendritic segment possessed an abundance of mitochondria and single-membrane organelles, such as SER and endosomes, and an electron-dense cytoplasm. These organelles are targeted to areas requiring greater energy production, Ca^{2+}

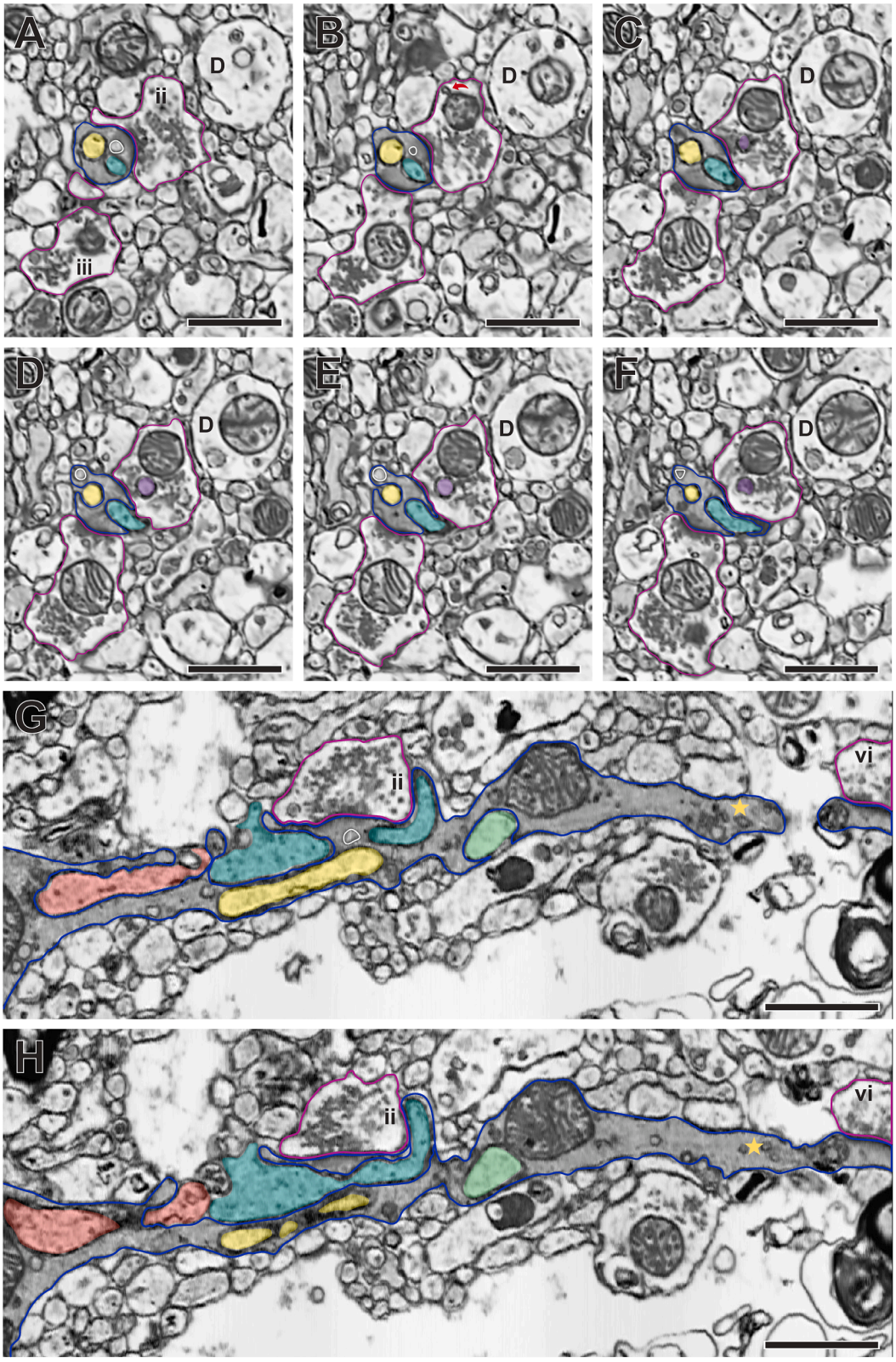

(legend on next page)

Table 1. Proportion of neuronal and glial compartments present in the densely reconstructed DLPFC layer 3 neuropil sub-volume

Cellular Compartment	Volume (μm^3)	% of total volume
Unmyelinated axons	19.1	29.7%
Dendritic shafts	15.6	24.3%
Astrocyte processes	9.3	14.4%
Axonal boutons	8.2	12.7%
Myelinated axons	3.0	4.7%
Dendritic spines	1.4	2.2%
Extracellular space	7.8	12.0%

buffering and regulation, and secretory trafficking of integral membrane proteins in order to support enhanced synaptic neurotransmission.[91] Furthermore, we also identified four discrete, invaginated filopodia-like structures situated within this dendrite's cytoplasm. These invaginating processes were not connected to any parent structure, instead presenting as independent entities within the dendritic shaft. Such a relationship suggests these processes were *trans*-endocytosed by the parent dendrite.[63] Recent studies using human PFC[74] or temporal lobe[76] biopsy samples for VEM also report the presence of filopodia-like structures within dendritic shafts, and we observed these filopodia-like structures occasionally in other dendritic shafts. Filopodia invaginating structures are implicated in synaptic formation, maintenance, pruning, and plasticity, and provide a unique means to further enhance the molecular, chemical, and morphological functional flexibility of the invaginated structure.[62,63,92–95] Thus, this dendritic segment possesses a repertoire of postsynaptic resources that enhance the capacity for localized synaptic integration and computation.[96,97]

FIB-SEM imaging with a 5-nm isotropic voxel size represented an ideal VEM approach to investigate and quantify *in situ* subcellular, synaptic, sub-synaptic, and organellar fine ultrastructural characteristics in brain tissue for this proof-of-principal study. Additionally, we demonstrated the utility of FIB-SEM imaging with a 20-nm isotropic voxel size for some experimental questions. Although lower resolution, this approach permitted the analysis of substantially larger volumes. FIB-SEM imaging with a 20-nm voxel size performed just as well as a 5-nm voxel size in quantifying Type 1 and Type 2 synaptic density, but identification of postsynaptic targets was superior in the 5 nm voxel size volume. However, experimental questions regarding finer ultrastructures, such as presynaptic active zones, PSDs, and mitochondrial cristae, are better suited to imaging approaches with a smaller axial step size. FIB-SEM may be particularly well-suited to these types of questions because (1) intact tissue samples are loaded into the FIB-SEM and are not moved between scans, mitigating risk of sample loss; (2) the isotropic 3D data from FIB-SEM avoids non-uniform anisotropic data across different tissue planes; (3) routine FIB-milling step sizes (e.g., 5–20 nm) are small in relation to many sub-cellular structures in the brain, minimizing loss of information[98–100]; and (4) once samples are loaded, FIB milling and SEM imaging can occur without manual operation. However, other VEM approaches, such as automated tape collection ultramicrotome (ATUM)[72] and serial block face SEM,[51] are also highly suitable for, and have demonstrated success in, investigations of brain tissue. The "quiet revolution" of VEM has resulted in a wealth of techniques that permit investigators to ask, and answer, fundamental questions about the ultrastructure of cells and tissues.[101]

In sum, the current findings provide proof-of-concept evidence that *in vivo* functioning of individual synapses in human brain can be investigated *ex vivo* in tissue obtained postmortem and analyzed by VEM. Our tissue processing workflow generated 3D datasets of excellent fixation, staining and ultrastructural preservation using samples with a PMI of 6.0 h and that were in storage for more than 8 years before staining and FIB-SEM imaging. This PMI is $\geq$2 h longer than other published VEM studies,[75,80,81] supporting that the workflow described here is compatible with longer PMIs. The success of our approach is also consistent with existing EM data demonstrating that ultrastructure is preserved, and light microscopic data of synaptic appositions, in postmortem human samples of longer PMIs [for examples, see[46,48,102–104]], and that PMI may not be the strongest predictor of ultrastructural preservation.[48] The suitability of both biopsy and autopsy human brain tissue samples, and of archived tissue samples, for quantitative VEM greatly expands the potential resource pool and opportunities to investigate ultrastructural correlates of neural function in human health and

Figure 7. A series of electron micrographs viewed in different coordinate planes illustrating the unique ultrastructural features of the complex dendritic shaft

(A–F) Electron micrographs spanning 315 nm in the XY coordinate plane illustrating two filopodia-like, invaginated structures (yellow and teal filled) completely enveloped within the dendritic shaft (dark blue outline) cytoplasm. The plasma membrane of the invaginated structures and the plasma membrane enclosing the dendritic cytoplasm are clearly distinct, and also show discrete, electron-dense regions which appear to be non-synaptic contacts. Unlike other dendritic profiles (D) in close proximity, the complex dendritic shaft exhibits a more electron-dense cytoplasm, indicative of an abundance of molecules involved in cellular, organelle and synaptic function. In (A), a single Type 1 synapse from axonal bouton ii (pink outline) is visible. Presumptive endosome large vesicle (white outline) is positioned between the PSD and the two invaginated structures. In (B), an additional Type 1 synapse is present on the dendritic shaft that is formed by axonal bouton iii. In axonal bouton ii (top), a mitochondrial-derived vesicle (red curved arrow) is visible. (C–F) illustrate the teal filopodia-like structure exiting the dendritic shaft, and the yellow filopodia-like structure partially exposed to the neuropil. (C–F) also show an invaginated structure (purple filled) piercing the cytoplasm of synaptic axonal bouton ii (top).

(G and H) Electron micrographs separated by 70 nm in the XZ coordinate plane illustrating the same dendritic shaft. The Type 1 synapse formed by bouton ii, and all four filopodia-like invaginated structures (salmon, teal, yellow, and lime green filled) are shown. A portion of axonal bouton vi is visible at the far right. The electron-dense dendritic cytoplasm is apparent, as is an abundance of putative endosomal and SER structures. A classic example of amorphous vesicular clumps (gold star) is present in the dendritic shaft. Amorphous vesicular clumps likely reflect a mix of SER and endosomal vesicles.[59] The yellow and teal invaginated structures and the endosome large vesicle (white outline) are visible in (G), positioned centrally to the PSD. D-dendrite. Scale bar is 1 μm.

Table 2. Synaptic bouton identity, density, and postsynaptic target present in the high- and low-resolution DLPFC layer 3 neuropil subvolumes

Imaging Resolution	Bouton Type	N	Density	Postsynaptic Target			
				Spine	Shaft	Axon	Unknown
High (5nm^3 voxel size)	Synaptic- Type 1	20	0.31/μm^3	14 (70%)	6 (30%)	0	0
	Synaptic- Type 2	5	0.08/μm^3	0	4 (80%)	1 (20%)	0
	Non-synaptic	3	0.05/μm^3	–	–	–	–
Low (20nm^3 voxel size)	Synaptic- Type 1	94	0.35/μm^3	45 (48%)	33 (35%)	0	16 (17%)
	Synaptic- Type 2	11	0.04/μm^3	5 (45%)	6 (55%)	0	0
	Non-synaptic	10	0.05/μm^3	–	–	–	–

disease. The current findings show that not only are these subsynaptic structures able to be identified, segmented, and reconstructed in 3D in postmortem human brain, but that the biological processes occurring postmortem do not affect fundamental pre- and postsynaptic relationships. Finally, our use of FIB-SEM technology has revealed a novel hub-like dendritic segment in human DLPFC with features of a "resource-rich" neuronal compartment suited for synaptic plasticity and information processing.[105] Together, these findings indicate that VEM imaging studies of postmortem human brain can be used to investigate the nature of synaptic dysfunction in brain disorders.

Limitations of the study

The current study is associated with some interpretative limitations. First, our analyses were completed in one subject, raising the possibility that results may not be generalizable to other subjects. Although the consistency of our results with existing EM studies in experimental model systems and previously published human brain tissue samples obtained via biopsy or postmortem (see introduction and discussion) suggests this likely is not the case; further studies with larger sample sizes are required. Second, quantitative VEM approaches provide an indirect way to study measures that index synaptic, sub-synaptic, and mitochondrial function. Neural communication is a dynamic process, and all microscopy studies of preserved brain tissue capture only a snapshot of these processes. Technologies with the resolving power to study the functioning of individual synapses in the *in vivo* human brain are not yet available. Indeed, synapse-specific functional assessments can be challenging even within *in vivo* animal models where invasive approaches are utilized.[106] Third, our analyses were restricted to the neuropil and, as such, we cannot definitively determine the location of a parent cell body for any given neuronal process such as an axon, bouton, dendrite, or spine. However, the cellular and neuropil composition of the DLPFC is well-studied,[107,108] and those findings support that (1) dendritic spines, and their parent dendritic shafts, emerge from local glutamatergic pyramidal neurons, (2) unmyelinated axons emerge from local neurons, (3) axonal boutons forming Type 1 synapses are most likely from local pyramidal neurons, but we cannot exclude that some may reflect long-range cortical inputs or thalamocortical inputs, and (4) axonal boutons forming Type 2 synapses are most likely from local GABAergic interneurons, but we cannot exclude that some may reflect inputs from other neurotransmitter systems such

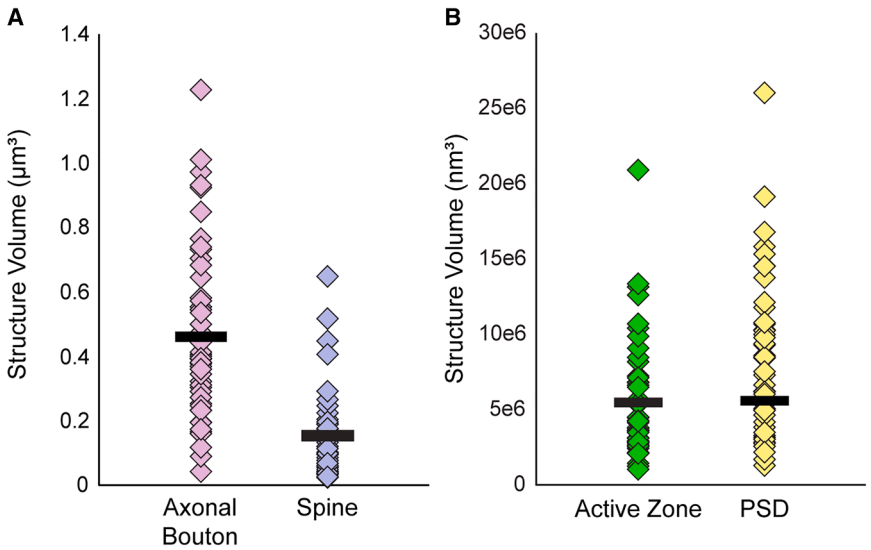

Figure 8. Scatterplots showing the volumes of each reconstructed synaptic and subsynaptic structure in postmortem human DLPFC layer 3

(A) Volumes of 50 Type 1 synaptic axonal boutons and the 50 postsynaptic spines.

(B) Volumes of the presynaptic active zones and PSDs. Markers represent an individual structure, and black bars represent the mean volume.

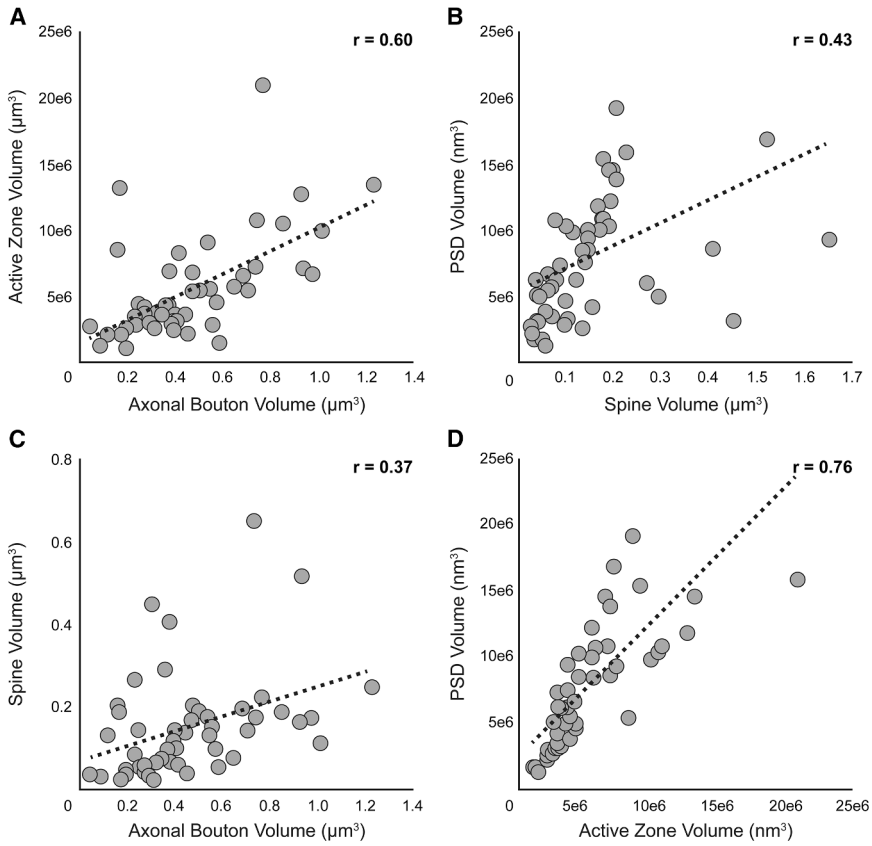

Figure 9. Correlation plots showing the relationships between Type 1 synaptic and sub-synaptic structures in postmortem human DLPFC layer 3

(A–D) Markers represent the volumes of each structure within an individual synapse. (A) Strong, positive correlation was identified between bouton and active zone volumes. (B) Moderate, positive correlation was identified between spine head and PSD volumes, as well as between (C) spine and PSD volumes. (D) Strong, positive correlation was identified between active zone and PSD volumes.

as dopamine. Fourth, we used a semi-automated segmentation approach that required some manual interaction. Future studies utilizing interactive deep-learning algorithms will accelerate dense segmentation and reconstruction of imaged volumes.[73,109,110] Finally, as with all studies of postmortem human brain tissue,[111,112] mitigating the effect of potential confounding factors is a key aspect of rigorous experimental design when interrogating the disease effects. In particular, our study highlights the importance of ensuring that objective measures of ultrastructural preservation and quality[48] do not differ between comparison and disease groups.

RESOURCE AVAILABILITY

Lead contact

Requests for further information and resources should be directed to and will be fulfilled by the lead contact, Jill R. Glausier (glausierjr@upmc.edu).

Materials availability

This study did not generate new unique reagents.

Data and code availability

- Data: All data reported in this paper will be shared by the lead contact upon request.
- Code: This paper does not report original code.
- Additional information: Any additional information required to reanalyze the data reported in this paper is available from the lead contact upon request.

ACKNOWLEDGMENTS

The authors gratefully acknowledge the digital graphics expertise of Mary Brady. Brain tissue was provided by the University of Pittsburgh Brain Tissue Donation Program. Funding support was provided by NIH grants R01MH132544 (J.R.G.), S10MH133575 (J.R.G. and Z.F.), R01DA061243 (Z.F.), R01ES034037 (Z.F.), R21AA028800 (Z.F.), Commonwealth of Pennsylvania Formula Fund (Z.F.), The Pittsburgh Foundation (Z.F.), and Baszucki Brain Research Funds (Z.F.). All data were previously published in preprint form on bioRxiv.com.

AUTHOR CONTRIBUTIONS

Conceptualization, J.R.G.; methodology, J.R.G., C.B.-M., K.W., and Z.F.; formal analysis, J.R.G.; investigation, J.R.G., C.B.-M., M.M., T.B.-T., K.W., J.N., and D.M.; resources, J.R.G., D.A.L., and Z.F.; data curation, J.R.G., M.M., T.B.-T., and D.M.; writing – original draft, J.R.G.; writing – review and editing, J.R.G., D.A.L., and Z.F.; visualization, J.R.G., C.B.-M., M.M., and K.W.; supervision, J.R.G. and D.A.L.; funding acquisition, J.R.G. and Z.F.

DECLARATION OF INTERESTS

D.A.L. currently receives investigator-initiated research support from Merck. Z.F. receives investigator-initiated research support from the University of Pittsburgh Medical Center (UPMC) Enterprises. C.B.-M. and K.W. are

Table 3. Comparison of synaptic, sub-synaptic and mitochondrial volumes based on mitochondrion abundance in Type 1 axo-spinous synapses

	# Mitochondria in synaptic axonal boutons			
Measure	0	1	≥2	Statistic[a]
# Boutons	24	22	4	–
Mitochondria Volume μm^3	–	0.10 ± 0.04	0.19 ± 0.08	–
Bouton volume μm^3	0.27 ± 0.14	0.51 ± 0.19	0.48 ± 0.19	$F_{1,48} = 24.8$ $p = 9.0e^{-6}$
Spine volume μm^3	0.12 ± 0.15	0.14 ± 0.09	0.17 ± 0.02	$F_{1,48} = 0.74$ $p = 0.4$
Active Zone volume nm^3	3.76 ± 2.60e^6	6.63 ± 4.23e^6	9.23 ± 3.22e^6	$F_{1,48} = 11.07$ $p = 0.002$
PSD volume nm^3	5.76 ± 4.16e^6	9.24 ± 4.20e^6	1.52 ± 3.38e^7	$F_{1,48} = 11.02$ $p = 0.002$
% Spines with an Apparatus or SER	33%	90%	100%	$\chi^2 = 11.0$ $p = 0.0009$

[a]For statistical comparisons, the independent measure was mitochondria presence (≥1, $n = 26$) or absence (0, $n = 24$) in axonal boutons. Values are counts or mean ± standard deviation.

employed by Thermo Fisher Scientific. J.R.G. and J.N. reported no biomedical financial interests or potential conflicts of interest. C.B.-T., D.M., and M.M. reported no biomedical financial interests or potential conflicts of interest.

STAR★METHODS

Detailed methods are provided in the online version of this paper and include the following:

- KEY RESOURCES TABLE
- EXPERIMENTAL MODEL AND STUDY PARTICIPANT DETAILS
- METHOD DETAILS
  - Sample preparation
  - FIB-SEM imaging
- QUANTIFICATION AND STATISTICAL ANALYSIS
  - Ultrastructural analysis
  - Statistics analyses

SUPPLEMENTAL INFORMATION

Supplemental information can be found online at https://doi.org/10.1016/j.isci.2025.112747.

Table 4. Comparison of synaptic, sub-synaptic and mitochondrial volumes in Type 1 axo-spinous synapses based on presence of a spine apparatus or SER

	Spine Apparatus/SER		
Measure	Yes	No	Statistic
# Spines	44	6	–
Bouton volume μm^3	0.41 ± 0.21	0.24 ± 0.11	$F_{1,48} = 3.72$, $p = 0.06$
Spine volume μm^3	0.15 ± 0.12	0.04 ± 0.03	$F_{1,48} = 4.47$, $p = 0.04$
Active Zone volume nm^3	5.91 ± 3.87e^6	2.25 ± 0.89e^6	$F_{1,48} = 5.22$, $p = 0.03$
PSD volume nm^3	8.61 ± 5.14e^6	3.45 ± 1.84e^6	$F_{1,48} = 6.01$, $p = 0.02$
% Boutons containing mitochondria	57%	17%	$\chi^2 = 3.4$ $p = 0.06$
Mitochondria volume μm^3	0.11 ± 0.06	0.10	$F_{1,48} = 0.005$, $p = 0.9$

Values are counts or mean ± standard deviation.

Received: September 7, 2024
Revised: March 15, 2025
Accepted: May 22, 2025
Published: May 26, 2025

REFERENCES

1. Ho, V.M., Lee, J.-A., and Martin, K.C. (2011). The cell biology of synaptic plasticity. Science *334*, 623–628.
2. Glausier, J.R., and Lewis, D.A. (2018). Mapping pathologic circuitry in schizophrenia. Handb. Clin. Neurol. *150*, 389–417. https://doi.org/10.1016/b978-0-444-63639-3.00025-6.
3. Howes, O.D., and Onwordi, E.C. (2023). The synaptic hypothesis of schizophrenia version III: a master mechanism. Mol. Psychiatry *28*, 1843–1856. https://doi.org/10.1038/s41380-023-02043-w.
4. Neniskyte, U., and Gross, C.T. (2017). Errant gardeners: glial-cell-dependent synaptic pruning and neurodevelopmental disorders. Nat. Rev. Neurosci. *18*, 658–670. https://doi.org/10.1038/nrn.2017.110.
5. Heuser, J.E., and Reese, T.S. (1973). Evidence for recycling of synaptic vesicle membrane during transmitter release at the frog neuromuscular junction. J. Cell Biol. *57*, 315–344. https://doi.org/10.1083/jcb.57.2.315.
6. Palay, S.L. (1964). The structural basis for neural action. In Brain Function: RNA and Brain Function, Memory and Learning, M.A.B. Brazier, ed. (University of California Press), pp. 69–100.
7. Holler, S., Köstinger, G., Martin, K.A.C., Schuhknecht, G.F.P., and Stratford, K.J. (2021). Structure and function of a neocortical synapse. Nature *591*, 111–116. https://doi.org/10.1038/s41586-020-03134-2.
8. Schikorski, T., and Stevens, C.F. (1997). Quantitative Ultrastructural Analysis of Hippocampal Excitatory Synapses. J. Neurosci. *17*, 5858–5867. https://doi.org/10.1523/jneurosci.17-15-05858.1997.
9. Matz, J., Gilyan, A., Kolar, A., McCarvill, T., and Krueger, S.R. (2010). Rapid structural alterations of the active zone lead to sustained changes in neurotransmitter release. Proc. Natl. Acad. Sci. USA *107*, 8836–8841. https://doi.org/10.1073/pnas.0906087107.
10. Maschi, D., and Klyachko, V.A. (2017). Spatiotemporal Regulation of Synaptic Vesicle Fusion Sites in Central Synapses. Neuron *94*, 65–73. e3. https://doi.org/10.1016/j.neuron.2017.03.006.
11. Südhof, T.C. (2012). The presynaptic active zone. Neuron *75*, 11–25. https://doi.org/10.1016/j.neuron.2012.06.012.
12. Takumi, Y., Ramírez-León, V., Laake, P., Rinvik, E., and Ottersen, O.P. (1999). Different modes of expression of AMPA and NMDA receptors in hippocampal synapses. Nat. Neurosci. *2*, 618–624. https://doi.org/10.1038/10172.
13. Shinohara, Y., Hirase, H., Watanabe, M., Itakura, M., Takahashi, M., and Shigemoto, R. (2008). Left-right asymmetry of the hippocampal synapses with differential subunit allocation of glutamate receptors. Proc.

Natl. Acad. Sci. USA *105*, 19498–19503. https://doi.org/10.1073/pnas.0807461105.

14. Fukazawa, Y., and Shigemoto, R. (2012). Intra-synapse-type and inter-synapse-type relationships between synaptic size and AMPAR expression. Curr. Opin. Neurobiol. *22*, 446–452. https://doi.org/10.1016/j.conb.2012.01.006.
15. Chen, X., Levy, J.M., Hou, A., Winters, C., Azzam, R., Sousa, A.A., Leapman, R.D., Nicoll, R.A., and Reese, T.S. (2015). PSD-95 family MAGUKs are essential for anchoring AMPA and NMDA receptor complexes at the postsynaptic density. Proc. Natl. Acad. Sci. USA *112*, E6983–E6992. https://doi.org/10.1073/pnas.1517045112.
16. Patriarchi, T., Buonarati, O.R., and Hell, J.W. (2018). Postsynaptic localization and regulation of AMPA receptors and Cav1.2 by β2 adrenergic receptor/PKA and Ca(2+)/CaMKII signaling. EMBO J. *37*, e99771. https://doi.org/10.15252/embj.201899771.
17. Rangaraju, V., Calloway, N., and Ryan, T.A. (2014). Activity-driven local ATP synthesis is required for synaptic function. Cell *156*, 825–835. https://doi.org/10.1016/j.cell.2013.12.042.
18. Ivannikov, M.V., Sugimori, M., and Llinás, R.R. (2013). Synaptic vesicle exocytosis in hippocampal synaptosomes correlates directly with total mitochondrial volume. J. Mol. Neurosci. *49*, 223–230. https://doi.org/10.1007/s12031-012-9848-8.
19. Attwell, D., and Laughlin, S.B. (2001). An energy budget for signaling in the grey matter of the brain. J. Cereb. Blood Flow Metab. *21*, 1133–1145. https://doi.org/10.1097/00004647-200110000-00001.
20. Hall, C.N., Klein-Flügge, M.C., Howarth, C., and Attwell, D. (2012). Oxidative phosphorylation, not glycolysis, powers presynaptic and postsynaptic mechanisms underlying brain information processing. J. Neurosci. *32*, 8940–8951.
21. Harris, J.J., Jolivet, R., and Attwell, D. (2012). Synaptic energy use and supply. Neuron *75*, 762–777. https://doi.org/10.1016/j.neuron.2012.08.019.
22. Howarth, C., Gleeson, P., and Attwell, D. (2012). Updated energy budgets for neural computation in the neocortex and cerebellum. J. Cereb. Blood Flow Metab. *32*, 1222–1232. https://doi.org/10.1038/jcbfm.2012.35.
23. Ma, H., Cai, Q., Lu, W., Sheng, Z.H., and Mochida, S. (2009). KIF5B motor adaptor syntabulin maintains synaptic transmission in sympathetic neurons. J. Neurosci. *29*, 13019–13029. https://doi.org/10.1523/jneurosci.2517-09.2009.
24. Verstreken, P., Ly, C.V., Venken, K.J.T., Koh, T.W., Zhou, Y., and Bellen, H.J. (2005). Synaptic mitochondria are critical for mobilization of reserve pool vesicles at Drosophila neuromuscular junctions. Neuron *47*, 365–378. https://doi.org/10.1016/j.neuron.2005.06.018.
25. Li, S., Xiong, G.J., Huang, N., and Sheng, Z.H. (2020). The cross-talk of energy sensing and mitochondrial anchoring sustains synaptic efficacy by maintaining presynaptic metabolism. Nat. Metab. *2*, 1077–1095. https://doi.org/10.1038/s42255-020-00289-0.
26. Seager, R., Lee, L., Henley, J.M., and Wilkinson, K.A. (2020). Mechanisms and roles of mitochondrial localisation and dynamics in neuronal function. Neuronal Signal. *4*, Ns20200008. https://doi.org/10.1042/ns20200008.
27. Justs, K.A., Lu, Z., Chouhan, A.K., Borycz, J.A., Lu, Z., Meinertzhagen, I. A., and Macleod, G.T. (2022). Presynaptic Mitochondrial Volume and Packing Density Scale with Presynaptic Power Demand. J. Neurosci. *42*, 954–967. https://doi.org/10.1523/jneurosci.1236-21.2021.
28. Li, S., and Sheng, Z.H. (2022). Energy matters: presynaptic metabolism and the maintenance of synaptic transmission. Nat. Rev. Neurosci. *23*, 4–22. https://doi.org/10.1038/s41583-021-00535-8.
29. Rossi, M.J., and Pekkurnaz, G. (2019). Powerhouse of the mind: mitochondrial plasticity at the synapse. Curr. Opin. Neurobiol. *57*, 149–155. https://doi.org/10.1016/j.conb.2019.02.001.
30. Mendelsohn, R., Garcia, G.C., Bartol, T.M., Lee, C.T., Khandelwal, P., Liu, E., Spencer, D.J., Husar, A., Bushong, E.A., Phan, S., et al. (2022). Morphological principles of neuronal mitochondria. J. Comp. Neurol. *530*, 886–902. https://doi.org/10.1002/cne.25254.
31. Hackenbrock, C.R. (1981). Energy-linked condensed-orthodox ultrastructural transformations in mitochondria. Chemotherapy *27*, 21–26.
32. Scalettar, B.A., Abney, J.R., and Hackenbrock, C.R. (1991). Dynamics, structure, and function are coupled in the mitochondrial matrix. Proc. Natl. Acad. Sci. USA *88*, 8057–8061.
33. Cserép, C., Pósfai, B., Schwarcz, A.D., and Dénes, Á. (2018). Mitochondrial Ultrastructure Is Coupled to Synaptic Performance at Axonal Release Sites. eNeuro *5*, 0390-0317.2018. https://doi.org/10.1523/eneuro.0390-17.2018.
34. Südhof, T.C., and Malenka, R.C. (2008). Understanding synapses: past, present, and future. Neuron *60*, 469–476. https://doi.org/10.1016/j.neuron.2008.10.011.
35. Di Maio, V. (2021). The glutamatergic synapse: a complex machinery for information processing. Cogn. Neurodyn. *15*, 757–781. https://doi.org/10.1007/s11571-021-09679-w.
36. Sanderson, T.M., Georgiou, J., and Collingridge, G.L. (2020). Illuminating Relationships Between the Pre- and Post-synapse. Front. Neural Circuits *14*, 9. https://doi.org/10.3389/fncir.2020.00009.
37. Smith, H.L., Bourne, J.N., Cao, G., Chirillo, M.A., Ostroff, L.E., Watson, D. J., and Harris, K.M. (2016). Mitochondrial support of persistent presynaptic vesicle mobilization with age-dependent synaptic growth after LTP. eLife *5*, e15275. https://doi.org/10.7554/eLife.15275.
38. Miller, E.K., and Cohen, J.D. (2001). An integrative theory of prefrontal cortex function. Annu. Rev. Neurosci. *24*, 167–202. https://doi.org/10.1146/annurev.neuro.24.1.167.
39. Fuster, J.M. (2001). The prefrontal cortex - an update: Time is of the essence. Neuron *30*, 319–333.
40. Donahue, C.J., Glasser, M.F., Preuss, T.M., Rilling, J.K., and Van Essen, D.C. (2018). Quantitative assessment of prefrontal cortex in humans relative to nonhuman primates. Proc. Natl. Acad. Sci. USA *115*, E5183–E5192. https://doi.org/10.1073/pnas.1721653115.
41. Spocter, M.A., Hopkins, W.D., Barks, S.K., Bianchi, S., Hehmeyer, A.E., Anderson, S.M., Stimpson, C.D., Fobbs, A.J., Hof, P.R., and Sherwood, C.C. (2012). Neuropil distribution in the cerebral cortex differs between humans and chimpanzees. J. Comp. Neurol. *520*, 2917–2929. https://doi.org/10.1002/cne.23074.
42. Liu, X., Han, D., Somel, M., Jiang, X., Hu, H., Guijarro, P., Zhang, N., Mitchell, A., Halene, T., Ely, J.J., et al. (2016). Disruption of an Evolutionarily Novel Synaptic Expression Pattern in Autism. PLoS Biol. *14*, e1002558. https://doi.org/10.1371/journal.pbio.1002558.
43. Ogawa, L.M., and Vallender, E.J. (2014). Evolutionary conservation in genes underlying human psychiatric disorders. Front. Hum. Neurosci. *8*, 283. https://doi.org/10.3389/fnhum.2014.00283.
44. Levchenko, A., Gusev, F., and Rogaev, E. (2023). The evolutionary origin of psychosis. Front. Psychiatry *14*, 1115929. https://doi.org/10.3389/fpsyt.2023.1115929.
45. Teffer, K., and Semendeferi, K. (2012). Chapter 9 - Human prefrontal cortex: Evolution, development, and pathology. In Prog. Brain Res., M.A. Hofman and D. Falk, eds. (Elsevier), pp. 191–218. https://doi.org/10.1016/B978-0-444-53860-4.00009-X.
46. Glausier, J.R., Datta, D., Fish, K.N., Chung, D.W., Melchitzky, D.S., and Lewis, D.A. (2021). Laminar Differences in the Targeting of Dendritic Spines by Cortical Pyramidal Neurons and Interneurons in Human Dorsolateral Prefrontal Cortex. Neuroscience *452*, 181–191. https://doi.org/10.1016/j.neuroscience.2020.10.022.
47. Rees, S. (1976). A quantitative electron microscopic study of the ageing human cerebral cortex. Acta Neuropathol. *36*, 347–362. https://doi.org/10.1007/BF00699640.

48. Glausier, J.R., Konanur, A., and Lewis, D.A. (2019). Factors Affecting Ultrastructural Quality in the Prefrontal Cortex of the Postmortem Human Brain. J. Histochem. Cytochem. *67*, 185–202. https://doi.org/10.1369/0022155418819481.

49. Glausier, J.R., Roberts, R.C., and Lewis, D.A. (2017). Ultrastructural analysis of parvalbumin synapses in human dorsolateral prefrontal cortex. J. Comp. Neurol. *525*, 2075–2089. https://doi.org/10.1002/cne.24171.

50. Kuwajima, M., Spacek, J., and Harris, K.M. (2013). Beyond counts and shapes: studying pathology of dendritic spines in the context of the surrounding neuropil through serial section electron microscopy. Neuroscience *251*, 75–89. https://doi.org/10.1016/j.neuroscience.2012.04.061.

51. Peddie, C.J., Genoud, C., Kreshuk, A., Meechan, K., Micheva, K.D., Narayan, K., Pape, C., Parton, R.G., Schieber, N.L., Schwab, Y., et al. (2022). Volume electron microscopy. Nat. Rev. Methods Primers *2*, 51. https://doi.org/10.1038/s43586-022-00131-9.

52. Hua, Y., Laserstein, P., and Helmstaedter, M. (2015). Large-volume en-bloc staining for electron microscopy-based connectomics. Nat. Commun. *6*, 7923. https://doi.org/10.1038/ncomms8923.

53. Melchitzky, D.S., Sesack, S.R., Pucak, M.L., and Lewis, D.A. (1998). Synaptic targets of pyramidal neurons providing intrinsic horizontal connections in monkey prefrontal cortex. J. Comp. Neurol. *390*, 211–224.

54. Pucak, M.L., Levitt, J.B., Lund, J.S., and Lewis, D.A. (1996). Patterns of intrinsic and associational circuitry in monkey prefrontal cortex. J. Comp. Neurol. *376*, 614–630.

55. Levitt, J.B., Lewis, D.A., Yoshioka, T., and Lund, J.S. (1993). Topography of pyramidal neuron intrinsic connections in macaque monkey prefrontal cortex (areas 9 and 46). J. Comp. Neurol. *338*, 360–376. https://doi.org/10.1002/cne.903380304.

56. Hara, Y., Yuk, F., Puri, R., Janssen, W.G.M., Rapp, P.R., and Morrison, J.H. (2014). Presynaptic mitochondrial morphology in monkey prefrontal cortex correlates with working memory and is improved with estrogen treatment. Proc. Natl. Acad. Sci. USA *111*, 486–491. https://doi.org/10.1073/pnas.1311310110.

57. Peters, A., Palay, S.L., and Webster, D.F. (1991). The Fine Structure of the Nervous System (Oxford University Press).

58. Nahirney, P.C., and Tremblay, M.-E. (2021). Brain Ultrastructure: Putting the Pieces Together. Front. Cell Dev. Biol. *9*, 629503. https://doi.org/10.3389/fcell.2021.629503.

59. Cooney, J.R., Hurlburt, J.L., Selig, D.K., Harris, K.M., and Fiala, J.C. (2002). Endosomal compartments serve multiple hippocampal dendritic spines from a widespread rather than a local store of recycling membrane. J. Neurosci. *22*, 2215–2224. https://doi.org/10.1523/jneurosci.22-06-02215.2002.

60. Kleinjan, M.S., Buchta, W.C., Ogelman, R., Hwang, I.-W., Kuwajima, M., Hubbard, D.D., Kareemo, D.J., Prikhodko, O., Olah, S.L., Gomez Wulschner, L.E., et al. (2023). Dually innervated dendritic spines develop in the absence of excitatory activity and resist plasticity through tonic inhibitory crosstalk. Neuron *111*, 362–371.e6. https://doi.org/10.1016/j.neuron.2022.11.002.

61. DeFelipe, J., and Fariñas, I. (1992). The pyramidal neuron of the cerebral cortex: Morphological and chemical characteristics of the synaptic inputs. Prog. Neurobiol. *39*, 563–607.

62. Fiala, J.C., Feinberg, M., Popov, V., and Harris, K.M. (1998). Synaptogenesis via dendritic filopodia in developing hippocampal area CA1. J. Neurosci. *18*, 8900–8911. https://doi.org/10.1523/jneurosci.18-21-08900.1998.

63. Spacek, J., and Harris, K.M. (2004). Trans-endocytosis via spinules in adult rat hippocampus. J. Neurosci. *24*, 4233–4241. https://doi.org/10.1523/jneurosci.0287-04.2004.

64. Shepherd, G.M., and Harris, K.M. (1998). Three-dimensional structure and composition of CA3→CA1 axons in rat hippocampal slices: implications for presynaptic connectivity and compartmentalization. J. Neurosci. *18*, 8300–8310. https://doi.org/10.1523/jneurosci.18-20-08300.1998.

65. Becker, N., Wierenga, C.J., Fonseca, R., Bonhoeffer, T., and Nägerl, U.V. (2008). LTD induction causes morphological changes of presynaptic boutons and reduces their contacts with spines. Neuron *60*, 590–597. https://doi.org/10.1016/j.neuron.2008.09.018.

66. Schmidt, H., Gour, A., Straehle, J., Boergens, K.M., Brecht, M., and Helmstaedter, M. (2017). Axonal synapse sorting in medial entorhinal cortex. Nature *549*, 469–475. https://doi.org/10.1038/nature24005.

67. Atwood, H.L., and Karunanithi, S. (2002). Diversification of synaptic strength: presynaptic elements. Nat. Rev. Neurosci. *3*, 497–516. https://doi.org/10.1038/nrn876.

68. Abbott, L.F., and Regehr, W.G. (2004). Synaptic computation. Nature *431*, 796–803. https://doi.org/10.1038/nature03010.

69. Scholl, B., and Fitzpatrick, D. (2020). Cortical synaptic architecture supports flexible sensory computations. Curr. Opin. Neurobiol. *64*, 41–45. https://doi.org/10.1016/j.conb.2020.01.013.

70. Barbey, A.K., Koenigs, M., and Grafman, J. (2013). Dorsolateral prefrontal contributions to human working memory. Cortex *49*, 1195–1205. https://doi.org/10.1016/j.cortex.2012.05.022.

71. Perez-Alvarez, A., Yin, S., Schulze, C., Hammer, J.A., Wagner, W., and Oertner, T.G. (2020). Endoplasmic reticulum visits highly active spines and prevents runaway potentiation of synapses. Nat. Commun. *11*, 5083. https://doi.org/10.1038/s41467-020-18889-5.

72. Chirillo, M.A., Waters, M.S., Lindsey, L.F., Bourne, J.N., and Harris, K.M. (2019). Local resources of polyribosomes and SER promote synapse enlargement and spine clustering after long-term potentiation in adult rat hippocampus. Sci. Rep. *9*, 3861. https://doi.org/10.1038/s41598-019-40520-x.

73. Shapson-Coe, A., Januszewski, M., Berger, D.R., Pope, A., Wu, Y., Blakely, T., Schalek, R.L., Li, P.H., Wang, S., Maitin-Shepard, J., et al. (2021). A connectomic study of a petascale fragment of human cerebral cortex. Preprint at: bioRxiv. https://doi.org/10.1101/2021.05.29.446289

74. Karlupia, N., Schalek, R.L., Wu, Y., Meirovitch, Y., Wei, D., Charney, A.W., Kopell, B.H., and Lichtman, J.W. (2023). Immersion Fixation and Staining of Multicubic Millimeter Volumes for Electron Microscopy-Based Connectomics of Human Brain Biopsies. Biol. Psychiatry *94*, 352–360. https://doi.org/10.1016/j.biopsych.2023.01.025.

75. Cano-Astorga, N., DeFelipe, J., and Alonso-Nanclares, L. (2021). Three-Dimensional Synaptic Organization of Layer III of the Human Temporal Neocortex. Cereb. Cortex *31*, 4742–4764. https://doi.org/10.1093/cercor/bhab120.

76. Rollenhagen, A., Walkenfort, B., Yakoubi, R., Klauke, S.A., Schmuhl-Giesen, S.F., Heinen-Weiler, J., Voortmann, S., Marshallsay, B., Palaz, T., Holz, U., et al. (2020). Synaptic Organization of the Human Temporal Lobe Neocortex as Revealed by High-Resolution Transmission, Focused Ion Beam Scanning, and Electron Microscopic Tomography. Int. J. Mol. Sci. *21*, 5558. https://doi.org/10.3390/ijms21155558.

77. Schmuhl-Giesen, S., Rollenhagen, A., Walkenfort, B., Yakoubi, R., Sätzler, K., Miller, D., von Lehe, M., Hasenberg, M., and Lübke, J.H.R. (2022). Sublamina-Specific Dynamics and Ultrastructural Heterogeneity of Layer 6 Excitatory Synaptic Boutons in the Adult Human Temporal Lobe Neocortex. Cereb. Cortex *32*, 1840–1865. https://doi.org/10.1093/cercor/bhab315.

78. Yakoubi, R., Rollenhagen, A., von Lehe, M., Miller, D., Walkenfort, B., Hasenberg, M., Sätzler, K., and Lübke, J.H. (2019). Ultrastructural heterogeneity of layer 4 excitatory synaptic boutons in the adult human temporal lobe neocortex. eLife *8*, e48373. https://doi.org/10.7554/eLife.48373.

79. Yakoubi, R., Rollenhagen, A., von Lehe, M., Shao, Y., Sätzler, K., and Lübke, J.H.R. (2019). Quantitative Three-Dimensional Reconstructions of Excitatory Synaptic Boutons in Layer 5 of the Adult Human Temporal Lobe Neocortex: A Fine-Scale Electron Microscopic Analysis. Cereb. Cortex *29*, 2797–2814. https://doi.org/10.1093/cercor/bhy146.

80. Cano-Astorga, N., Plaza-Alonso, S., DeFelipe, J., and Alonso-Nanclares, L. (2024). Volume electron microscopy analysis of synapses in primary regions of the human cerebral cortex. Cereb. Cortex *34*, bhae312. https://doi.org/10.1093/cercor/bhae312.

81. Cano-Astorga, N., Plaza-Alonso, S., DeFelipe, J., and Alonso-Nanclares, L. (2023). 3D synaptic organization of layer III of the human anterior cingulate and temporopolar cortex. Cereb. Cortex *33*, 9691–9708. https://doi.org/10.1093/cercor/bhad232.

82. Domínguez-Álvaro, M., Montero-Crespo, M., Blazquez-Llorca, L., DeFelipe, J., and Alonso-Nanclares, L. (2019). 3D Electron Microscopy Study of Synaptic Organization of the Normal Human Transentorhinal Cortex and Its Possible Alterations in Alzheimer's Disease. eNeuro *6*, ENEURO.0140-19.2019. https://doi.org/10.1523/eneuro.0140-19.2019.

83. Domínguez-Álvaro, M., Montero-Crespo, M., Blazquez-Llorca, L., DeFelipe, J., and Alonso-Nanclares, L. (2021). 3D Ultrastructural Study of Synapses in the Human Entorhinal Cortex. Cereb. Cortex *31*, 410–425. https://doi.org/10.1093/cercor/bhaa233.

84. Domínguez-Álvaro, M., Montero-Crespo, M., Blazquez-Llorca, L., Insausti, R., DeFelipe, J., and Alonso-Nanclares, L. (2018). Three-dimensional analysis of synapses in the transentorhinal cortex of Alzheimer's disease patients. Acta Neuropathol. Commun. *6*, 20. https://doi.org/10.1186/s40478-018-0520-6.

85. Domínguez-Álvaro, M., Montero-Crespo, M., Blazquez-Llorca, L., Plaza-Alonso, S., Cano-Astorga, N., DeFelipe, J., and Alonso-Nanclares, L. (2021). 3D Analysis of the Synaptic Organization in the Entorhinal Cortex in Alzheimer's Disease. eNeuro *8*, ENEURO.0140-19.2019. https://doi.org/10.1523/eneuro.0504-20.2021.

86. Dumitriu, D., Hao, J., Hara, Y., Kaufmann, J., Janssen, W.G.M., Lou, W., Rapp, P.R., and Morrison, J.H. (2010). Selective changes in thin spine density and morphology in monkey prefrontal cortex correlate with aging-related cognitive impairment. J. Neurosci. *30*, 7507–7515.

87. Krassner, M.M., Kauffman, J., Sowa, A., Cialowicz, K., Walsh, S., Farrell, K., Crary, J.F., and McKenzie, A.T. (2023). Postmortem changes in brain cell structure: a review. Free Neuropathol. *4*, 10. https://doi.org/10.17879/freeneuropathology-2023-4790.

88. Roberts, R.C., Gaither, L.A., Peretti, F.J., Lapidus, B., and Chute, D.J. (1996). Synaptic organization of the human striatum: a postmortem ultrastructural study. J. Comp. Neurol. *374*, 523–534. https://doi.org/10.1002/(sici)1096-9861(19961028)374:4<523::Aid-cne4>3.0.Co;2-3.

89. Devine, M.J., and Kittler, J.T. (2018). Mitochondria at the neuronal presynapse in health and disease. Nat. Rev. Neurosci. *19*, 63–80. https://doi.org/10.1038/nrn.2017.170.

90. MacAskill, A.F., Atkin, T.A., and Kittler, J.T. (2010). Mitochondrial trafficking and the provision of energy and calcium buffering at excitatory synapses. Eur. J. Neurosci. *32*, 231–240.

91. Harris, K.M., and Weinberg, R.J. (2012). Ultrastructure of synapses in the mammalian brain. Cold Spring Harb. Perspect. Biol. *4*, a005587. https://doi.org/10.1101/cshperspect.a005587.

92. Petralia, R.S., Yao, P.J., Kapogiannis, D., and Wang, Y.X. (2021). Invaginating Structures in Synapses - Perspective. Front. Synaptic Neurosci. *13*, 685052. https://doi.org/10.3389/fnsyn.2021.685052.

93. Petralia, R.S., Wang, Y.X., Mattson, M.P., and Yao, P.J. (2018). Invaginating Structures in Mammalian Synapses. Front. Synaptic Neurosci. *104*, 4. https://doi.org/10.3389/fnsyn.2018.00004.

94. Campbell, C., Lindhartsen, S., Knyaz, A., Erisir, A., and Nahmani, M. (2020). Cortical Presynaptic Boutons Progressively Engulf Spinules as They Mature. eNeuro *7*, ENEURO.0426-19.2020. https://doi.org/10.1523/eneuro.0426-19.2020.

95. Zaccard, C.R., Gippo, I., Song, A., Geula, C., and Penzes, P. (2023). Dendritic spinule-mediated structural synaptic plasticity: Implications for development, aging, and psychiatric disease. Front. Mol. Neurosci. *16*, 1059730. https://doi.org/10.3389/fnmol.2023.1059730.

96. Lafourcade, M., van der Goes, M.S.H., Vardalaki, D., Brown, N.J., Voigts, J., Yun, D.H., Kim, M.E., Ku, T., and Harnett, M.T. (2022). Differential dendritic integration of long-range inputs in association cortex via subcellular changes in synaptic AMPA-to-NMDA receptor ratio. Neuron *110*, 1532–1546.e4. https://doi.org/10.1016/j.neuron.2022.01.025.

97. Fischer, L., Mojica Soto-Albors, R., Tang, V.D., Bicknell, B., Grienberger, C., Francioni, V., Naud, R., Palmer, L.M., and Takahashi, N. (2022). Dendritic Mechanisms for In Vivo Neural Computations and Behavior. J. Neurosci. *42*, 8460–8467. https://doi.org/10.1523/jneurosci.1132-22.2022.

98. Briggman, K.L., and Bock, D.D. (2012). Volume electron microscopy for neuronal circuit reconstruction. Curr. Opin. Neurobiol. *22*, 154–161. https://doi.org/10.1016/j.conb.2011.10.022.

99. Titze, B., and Genoud, C. (2016). Volume scanning electron microscopy for imaging biological ultrastructure. Biol. Cell *108*, 307–323. https://doi.org/10.1111/boc.201600024.

100. Denk, W., and Horstmann, H. (2004). Serial block-face scanning electron microscopy to reconstruct three-dimensional tissue nanostructure. PLoS Biol. *2*, e329. https://doi.org/10.1371/journal.pbio.0020329.

101. Collinson, L.M., Bosch, C., Bullen, A., Burden, J.J., Carzaniga, R., Cheng, C., Darrow, M.C., Fletcher, G., Johnson, E., Narayan, K., et al. (2023). Volume EM: a quiet revolution takes shape. Nat. Methods *20*, 777–782. https://doi.org/10.1038/s41592-023-01861-8.

102. Glausier, J.R., Fish, K.N., and Lewis, D.A. (2014). Altered parvalbumin basket cell inputs in the dorsolateral prefrontal cortex of schizophrenia subjects. Mol. Psychiatry *19*, 30–36. https://doi.org/10.1038/mp.2013.152.

103. Kay, K.R., Smith, C., Wright, A.K., Serrano-Pozo, A., Pooler, A.M., Koffie, R., Bastin, M.E., Bak, T.H., Abrahams, S., Kopeikina, K.J., et al. (2013). Studying synapses in human brain with array tomography and electron microscopy. Nat. Protoc. *8*, 1366–1380. https://doi.org/10.1038/nprot.2013.078.

104. Sele, M., Wernitznig, S., Lipovšek, S., Radulović, S., Haybaeck, J., Birkl-Toeglhofer, A.M., Wodlej, C., Kleinegger, F., Sygulla, S., Leoni, M., et al. (2019). Optimization of ultrastructural preservation of human brain for transmission electron microscopy after long post-mortem intervals. Acta Neuropathol. Commun. *7*, 144. https://doi.org/10.1186/s40478-019-0794-3.

105. Harris, K.M. (2020). Synaptic Odyssey. J. Neurosci. *40*, 61–80. https://doi.org/10.1523/jneurosci.0735-19.2019.

106. Lines, J., Covelo, A., Gómez, R., Liu, L., and Araque, A. (2017). Synapse-Specific Regulation Revealed at Single Synapses Is Concealed When Recording Multiple Synapses. Front. Cell. Neurosci. *11*, 367. https://doi.org/10.3389/fncel.2017.00367.

107. White, E.L. (1989). Cortical Circuits. Synaptic Organization of the Cerebral Cortex. In Structure, Function and Theory (Birkhäuser).

108. (1990). The Prefrontal Cortex: Its Structure. In Function and Pathology, H.B.M. Uylings, C.G. Van Eden, J.P.C. De Bruin, M.A. Corner, and M.G.P. Feenstra, eds. (Elsevier).

109. Suga, S., Nakamura, K., Nakanishi, Y., Humbel, B.M., Kawai, H., and Hirabayashi, Y. (2023). An interactive deep learning-based approach reveals mitochondrial cristae topologies. PLoS Biol. *21*, e3002246. https://doi.org/10.1371/journal.pbio.3002246.

110. Conrad, R., and Narayan, K. (2023). Instance segmentation of mitochondria in electron microscopy images with a generalist deep learning model trained on a diverse dataset. Cell Syst. *14*, 58–71.e5. https://doi.org/10.1016/j.cels.2022.12.006.

111. Beneyto, M., Sibille, E., and Lewis, D.A. (2009). Human postmortem brain research in mental illness syndromes. In Neurobiology of Mental Illness, D.S. Charney and E.J. Nestler, eds. (Oxford University Press), pp. 202–214.

112. Bao, A.M., and Swaab, D.F. (2018). The art of matching brain tissue from patients and controls for postmortem research. Handb. Clin. Neurol. *150*, 197–217. https://doi.org/10.1016/b978-0-444-63639-3.00015-3.

113. Glantz, L.A., and Lewis, D.A. (2000). Decreased dendritic spine density on prefrontal cortical pyramidal neurons in schizophrenia. Arch. Gen. Psychiatry *57*, 65–73. https://doi.org/10.1001/archpsyc.57.1.65.

114. Glausier, J.R., Kelly, M.A., Salem, S., Chen, K., and Lewis, D.A. (2020). Proxy measures of premortem cognitive aptitude in postmortem subjects with schizophrenia. Psychol. Med. *50*, 507–514. https://doi.org/10.1017/s0033291719000382.

115. Luft, J.H. (1961). Improvements in epoxy resin embedding methods. J. Biophys. Biochem. Cytol. *9*, 409–414. https://doi.org/10.1083/jcb.9.2.409.

116. Wanner, A.A., Genoud, C., and Friedrich, R.W. (2016). 3-dimensional electron microscopic imaging of the zebrafish olfactory bulb and dense reconstruction of neurons. Sci. Data *3*, 160100. https://doi.org/10.1038/sdata.2016.100.

117. Gray, E.G. (1959). Axo-somatic and axo-dendritic synapses of the cerebral cortex: An electron microscopic study. J. Anat. *93*, 420–433.

118. Colonnier, M. (1981). The electron-microscopic analysis of the neuronal organization of the cerebral cortex. In The Organization of the Cerebral Cortex, F.O. Schmidt, F.G. Worden, G. Adelman, and S.G. Dennis, eds. (MIT Press), pp. 125–152.

119. Merchán-Pérez, A., Rodriguez, J.R., Alonso-Nanclares, L., Schertel, A., and Defelipe, J. (2009). Counting Synapses Using FIB/SEM Microscopy: A True Revolution for Ultrastructural Volume Reconstruction. Front. Neuroanat. *3*, 18. https://doi.org/10.3389/neuro.05.018.2009.

120. A. Peters and E.G. Jones, eds. (1984). Cerebral Cortex: Cellular Components of the Cerebral Cortex (Plenum Press).

121. Akert, K., Moor, H., and Pfenninger, K. (1971). Synaptic fine structure. Adv. Cytopharmacol. *1*, 273–290.

122. Perkins, G., Renken, C., Martone, M.E., Young, S.J., Ellisman, M., and Frey, T. (1997). Electron Tomography of Neuronal Mitochondria: Three-Dimensional Structure and Organization of Cristae and Membrane Contacts. J. Struct. Biol. *119*, 260–272. https://doi.org/10.1006/jsbi.1997.3885.

123. Glancy, B., Kim, Y., Katti, P., and Willingham, T.B. (2020). The Functional Impact of Mitochondrial Structure Across Subcellular Scales. Front. Physiol. *11*, 541040. https://doi.org/10.3389/fphys.2020.541040.

124. Liu, X., and Hajnóczky, G. (2011). Altered fusion dynamics underlie unique morphological changes in mitochondria during hypoxia-reoxygenation stress. Cell Death Differ. *18*, 1561–1572. https://doi.org/10.1038/cdd.2011.13.

125. Ahmad, T., Aggarwal, K., Pattnaik, B., Mukherjee, S., Sethi, T., Tiwari, B. K., Kumar, M., Micheal, A., Mabalirajan, U., Ghosh, B., et al. (2013). Computational classification of mitochondrial shapes reflects stress and redox state. Cell Death Dis. *4*, e461. https://doi.org/10.1038/cddis.2012.213.

126. Parker, P., Kuwajima, M., and Harris, K.M. (2019). SER and Spine Apparatus Identification. https://synapseweb.clm.utexas.edu/.

127. Spacek, J., and Harris, K.M. (1997). Three-Dimensional Organization of Smooth Endoplasmic Reticulum in Hippocampal CA1 Dendrites and Dendritic Spines of the Immature and Mature Rat. J. Neurosci. *17*, 190–203. https://doi.org/10.1523/jneurosci.17-01-00190.1997.

128. Špaček, J. (1985). Three-dimensional analysis of dendritic spines. Anat. Embryol. *171*, 235–243. https://doi.org/10.1007/BF00341418.

STAR★METHODS

KEY RESOURCES TABLE

REAGENT or RESOURCE	SOURCE	IDENTIFIER
Biological samples		
Postmortem human brain specimen	Allegheny County Office of the Medical Examiner	N/A
Chemicals, peptides, and recombinant proteins		
Glutaraldehyde	Electron Microscopy Sciences	Cat#16210
Paraformaldehyde	Electron Microscopy Sciences	Cat#15710
Glycerol	Thermo Fisher Scientific	Cat#A16205.0F
Ethylene glycol	Thermo Fisher Scientific	Cat#146750025
Sodium hydroxide	Thermo Fisher Scientific	Cat#A16037.36
Sodium phosphate monobasic	Thermo Fisher Scientific	Cat# 448170010
Sodium cacodylate trihydrate	Electron Microscopy Sciences	Cat#12300
OsO_4	Electron Microscopy Sciences	Cat#19150
Potassium hexacyanoferrate trihydrate	Electron Microscopy Sciences	Cat#20150
Thiocarbohydrazide	Electron Microscopy Sciences	Cat#21900
Uranyl acetate	Electron Microscopy Sciences	Cat#22400
Lead nitrate	Electron Microscopy Sciences	Cat#17900
L- aspartic acid	Thermo Fisher Scientific	Cat#12300
Liquid release agent	Electron Microscopy Sciences	Cat#70880
Propylene oxide	Electron Microscopy Sciences	Cat#20401
EMS EMbed 812	Electron Microscopy Sciences	Cat#14900
Araldite 502	Electron Microscopy Sciences	Cat#13900
Dodecenyl succinic anhydride	Electron Microscopy Sciences	Cat#13700
N-Benzyl-N, N-Dimethylamine	Electron Microscopy Sciences	Cat#11400
Software and algorithms		
Amira software	Thermo Fisher Scientific	RRID:SCR_007353
SPSS software	IBM	Version 27
Auto Slice and View 4.2 Software	Thermos Fisher Scientific	Cat#1111905
Other		
Vibratome	Leica	VT 1000P; RRID:SCR_016495
Ultramicrotome	Leica	Leica Ultracut UCT; RRID:SCR_020234
Histology diamond knife	Diatome	40-HI
Silver Paste	Ted Pella	Cat#16062
Focused Ion Beam Scanning Electron Microscope	Thermo Fisher Scientific	Helios 5 CX
Iridium	Leica	Cat#16771560

EXPERIMENTAL MODEL AND STUDY PARTICIPANT DETAILS

The brain specimen was obtained during a routine autopsy conducted at the Allegheny County Office of the Medical Examiner (Pittsburgh, PA) after consent for donation was obtained from the next-of-kin. An independent committee of experienced research clinicians confirmed the absence of any lifetime psychiatric or neurologic diagnoses for the decedent based on medical records, neuropathology examinations, toxicology reports, and structured diagnostic interviews conducted with family members of the decedent.[113,114] This subject was a 62-year-old male who died suddenly and out-of-hospital with an accidental manner of death. The postmortem interval (PMI, defined as the time elapsed between death and brain tissue preservation) was 6.0 h. PFC pH was measured as 7.0, and RNA Integrity Number measured as 8.7. These demographic and tissue features are within the range of our previously published light and EM studies of postmortem human brain tissue.[46,48,49,102] All procedures were approved by the

University of Pittsburgh's Committee for the Oversight of Research and Clinical Training Involving Decedents and the Institutional Review Board for Biomedical Research.

METHOD DETAILS

Sample preparation

A tissue block approximately 1 cm^3 in size, containing cortical layers 1–6 and the underlying white matter, was dissected fresh from the middle frontal gyrus, dorsolateral prefrontal cortex (DLPFC) Brodmann Area 46 (BA46). The tissue block was immersed in 4% paraformaldehyde/0.2% glutaraldehyde (made in 0.1M phosphate buffer [PB]) for 24 h at room temperature, followed by 24 h at 4°C in the fixative solution. The fixed tissue block was sectioned with a 50 μm step-size on a vibratome (VT 1000P, Leica, Wetzlar, Germany). Each section was immediately transferred into a single well of a 24-well plate filled with chilled cryoprotectant solution (30% ethylene glycol/30% glycerol). Trays were stored at −30°C until time for EM sample preparation.

Tissue sections underwent processing using an approach developed by Hua et al.,[52] that was modified to optimize preservation, staining and contrast for postmortem human brain tissue sections. Our approach for tissue extraction, fixation, sampling, and long-term preservation substantially differed from the Hua et al. original protocol, which was designed for staining of larger-volume mouse cortex.[52] Specifically, the Hua et al. protocol collected brain tissue following transcardial perfusion of fixative buffer containing 2.5% paraformaldehyde and 1.25% glutaraldehyde, before post-extraction fixation for 24h at 4°C. In contrast, the current study employed immersion fixation since transcardial perfusion is not feasible for postmortem human brain research. We also used a lower concentration of glutaraldehyde to minimize the potential for reduced tissue antigenicity for potential future immunohistochemistry studies. For brain tissue sampling, the original Hua et al. protocol used biopsy punches of 1 mm diameter and 2 mm in length, whereas we used sections cut at 50 μm thickness to ensure that staining occurred through the entire depth of the section. Finally, given the nature and parameters of postmortem human brain tissue research, donated tissue is immediately processed and preserved using approaches that ensure long-term storage will not deleteriously affect tissue integrity. Images and data presented in the current manuscript were obtained from a tissue slice that was prepared, preserved and stored in these conditions for 8.15 years.

The preparation began with the formulation of 0.1M PB by diluting a 0.24M stock solution, created from 8 g of sodium hydroxide (NaOH) and 33.7 g of sodium phosphate monobasic ($NaH_2PO_4 \cdot H_2O$) in 1 L of MilliQ water (MQW). For a final volume of 1 L, 416 mL of the stock solution was combined with 584 mL of MQW. A separate 0.15M Cacodylate Buffer (CB) was prepared by dissolving 32.1 g of sodium cacodylate trihydrate in 1 L of MQW. Next, a 2% osmium tetroxide (OsO_4) solution was prepared by mixing 5mL of 4% OsO_4 stock solution with 5mL of 0.15M CB. Tissue sections were rinsed twice in 0.1M PB for 5 min each, followed by three 5-min washes in 0.15M CB. Sections were then incubated in the prepared 2% OsO_4 solution for 90 min at room temperature, ensuring they remained flat using a glass rod. A 2.5% potassium ferrocyanide solution was made by dissolving 375 mg of potassium hexacyanoferrate trihydrate in 15 mL of 0.15M CB. After removing the OsO_4, sections were incubated in 2.5% potassium ferrocyanide for 90 min at room temperature. Post-incubation, sections underwent three washes in MQW: a 5-min rinse in a watch glass, followed by 30- and 90-min washes in a 6-well plate. Meanwhile, thiocarbohydrazide (TCH) solution was prepared by dissolving 0.2 g of TCH in 20 mL of deionized water, heating it to 60°C with stirring for 1 h, and filtering through a 0.22 μm syringe filter. Sections were then incubated in the filtered TCH solution for 45 min at 40°C, followed by two 30-min washes in MQW. Subsequent to washing, sections were incubated in a 1:1 solution of 2% OsO_4 to MQW for 90 min at room temperature. Finally, sections were incubated in a 1% uranyl acetate solution overnight at 4°C. The protocol resumed with the preparation of a fresh 1% uranyl acetate solution. Sections were incubated at 50°C in this solution for 120 min, then rinsed in MQW for 30 min. A lead aspartate solution was prepared by dissolving 132 mg of lead nitrate in 20 mL of an aspartic acid stock solution, which was heated to 60°C for 30 min, ensuring no precipitate formed. Sections were incubated in the lead aspartate solution for 120 min at 50°C.

Modifications to the dehydration and embedding steps were also introduced, including dehydration at room temperature rather than at 4°C, and employing a different resin mixture (Electron Microscopy Sciences [EMS], Hatfield, PA, USA) containing EMbed 812, Araldite GY 502, DDSA (Dodecenyl Succinic Anhydride) and BMDA (N-Benzyl-N, N-Dimethylamine) which utilizes propylene oxide, rather than acetone, as the final dehydrant.[115] Specifically, embedding Epon resin was prepared by combining 12.5 mL of Embed-812 resin, 7.5 mL of Araldite 502 plasticizer, 27.5 mL of DDSA hardener, and 1.3 mL of BDMA accelerator. The mixture was stirred gently to prevent bubble formation. Before embedding, sections underwent two 30-minute washes in MQW, followed by ethanol dehydration in increasing concentrations (50%, 70%, 95%, and 100%) for 5 and 15 minutes each. Dehydration was completed with two 15-minute incubations in propylene oxide. Sections were then incubated overnight in a 1:1 mixture of propylene oxide and Epon resin. The following day, sections were placed in 100% Epon resin for 3 hours at room temperature. Sections were then mounted onto slides coated with liquid release agent (Electron Microscopy Sciences), and polymerized in an oven at 60°C for two days. These modifications preserved the benefits of the Hua et al.[52] approach, including a staining intensity of sufficiently high contrast to visualize neuropil components via FIB-SEM and maintenance of staining intensity throughout the depth of the tissue section. After sample preparation, a ~2 mm x 2 mm sample of cortical layer 3 was dissected and adhered to an Epon resin capsule. Using a Leica Ultracut UCT ultramicrotome, excess resin was trimmed with a diamond knife (Histo Diamond Knife, Diatome, Switzerland) until the face of the tissue was visible.

FIB-SEM imaging

The tissue sample was milled and imaged using a Helios 5 CX FIB-SEM (Thermo Fisher Scientific). After mounting on an SEM stub with silver paste, the sample was coated with 5 nm Ir for enhanced conductivity. Carbon was deposited to protect the tissue sample, and front and side trenches were milled for cross section imaging. Electron beam and ion beam fiducial markers were prepared for milling and imaging alignment. Gallium ion FIB milling and scanning electron microscopic imaging were completed for two separate volumes: high resolution (5 nm^3 voxel size) and low resolution (20 nm^3 voxel size). Gallium ion FIB milling and electron microscopy were conducted at a 52°C stage tilt using Auto Slice and View 4.2 Software for both volumes. For the high-resolution volume, FIB milling conditions were 30 kV, 0.43 nA with a slice thickness set at 5 nm. The final high-resolution backscatter electron imaging was performed at 2 kV and 0.4 nA, with a 4 μs dwell time per pixel, using the In-column detector (ICD) under immersion mode. The final image dimensions were 4055 x 3278 pixels, with a 5 nm pixel resolution. A total number of 1,580 ortho-slices were acquired at 5 nm isotropic voxels to generate a complete volume of 2,630 μm^3 with dimensions 20.3 × 16.4 × 7.9 μm. The low-resolution volume was imaged from the same tissue sample using a slice thickness and pixel size four times greater than the primary volume, 20 × 20 × 20 nm. This approach permits analysis of substantially larger tissue volumes, which require a notably shorter collection time, but have lower resolution. FIB milling conditions were 30 kV, 2.4 nA FIB slice current with a slice thickness set at 20 nm. The final high-resolution backscatter electron imaging was performed at 2 kV and 0.4 nA beam current with a 5 μs dwell time per pixel, using through-the-lens detector (TLD) under immersion mode. The final image dimensions were 2132 x 1269 pixels, with a 20 nm pixel resolution.

QUANTIFICATION AND STATISTICAL ANALYSIS

Ultrastructural analysis

A sub-volume of neuropil (64.2 μm^3 with dimensions 6275 × 4095 × 2500 nm) that excluded cell bodies and vascular structures was extracted from the master high-resolution volume. Every neuronal and glial sub-cellular structure in this volume was segmented and reconstructed in 3D , an approach termed dense reconstruction,[116] using a semi-automated approach via Amira software. The plasma membrane of each cellular structure was manually segmented in the first, middle and last ortho-slices in the XY plane. The Interpolation deep-learning module was then applied to segment the remaining plasma membrane of the structure. The operator evaluated, and corrected where needed, the segmentation in all perspective planes (XY, XZ, YZ). Because FIB-SEM imaging generates micrographic datasets with isotropic voxels, resolution is maintained in all perspective planes. As such, a 3D reconstruction of every cellular structure within the sub-volume was generated with 5 nm isotropic voxel resolution. Each segmented cellular structure was evaluated in 3D and annotated as neuronal dendritic shafts, dendritic spines, axonal boutons, unmyelinated axons, myelinated axons, or glial processes using well-established ultrastructural criteria.[57,117–120]

Neuronal synaptic complexes were also identified using well-established ultrastructural criteria,[57,117–120] and Type 1 and Type 2 synaptic densities were calculated in the densely reconstructed sub-volume (64.2 μm^3). Type 1 glutamatergic synapses were defined by a presynaptic axonal bouton directly apposed to a postsynaptic element. The postsynaptic element possessed a PSD, the electron-dense region characteristic of glutamate synapses that contains the postsynaptic proteins required for glutamatergic synaptic signaling.[91] The presynaptic bouton possessed a presynaptic active zone, defined as the electron-dense and synaptically-engaged region of the axonal bouton.[121] The pre- and postsynaptic compartments were separated by a distinct synaptic cleft.[117] Type 2, non-glutamatergic synapses were identified as described above, except the postsynaptic element did not contain a PSD, but instead exhibited greater plasma membrane electron density in the area apposed to the bouton relative to surrounding membrane. Synapses were first identified and annotated in the XY plane, then the XZ and YZ planes were evaluated to ensure that synaptic complexes were included in the synaptic density calculations, irrespective of the angle of the cut.

A sub-volume of neuropil (270 μm^3 with dimensions 750 × 300 × 150 nm) that excluded cell bodies and vascular structures was extracted from the master low-resolution volume. We evaluated whether Type 1 and Type 2 synapses could be reliably identified at a lower anatomical resolution as an initial test of the suitability of lower resolution volumes for synaptic analysis. Neuronal synaptic complexes were identified and quantified as described above.

A targeted analysis of 50 Type 1 axo-spinous synapses was separately completed to obtain detailed volumetric measurements of glutamatergic synaptic and sub-synaptic components at high resolution. Because the entirety of the synaptic complex was required to be present in X, Y, and Z dimensions for this analysis, the master volume (2,630 μm^3) was evaluated for Type 1 synapses. Using a random Z-plane start, 50 Type 1 axo-spinous synapses were systematically randomly identified in the XY plane using the above-described criteria. The axonal bouton, spine head, presynaptic active zone and PSD were fully reconstructed in 3D to obtain individual ultrastructural volumes. Each Type 1 axo-spinous synapse was evaluated for the presence of presynaptic mitochondria in boutons. Mitochondria were defined as discrete organelles identified by well-established ultrastructural criteria,[57,122] including the presence of a double membrane (comprised of mitochondrial inner and outer membranes), internal cristae membranes, and a matrix. Mitochondrial abundance,[25,27,28] size[27,29] and morphology[30–33] inform the relative level of activity at individual synapses.[89,123] The number of presynaptic mitochondria was tallied, and the volume of each was obtained via segmentation and 3D reconstruction. All mitochondria were classified as exhibiting globular, elongated, toroid (i.e., doughnut-shaped) or damaged morphology.[30,48,56] Toroid and damaged morphologies are associated with mitochondrial dysfunction *per se*,[124,125] and we did not observe any presynaptic mitochondria with these morphological characteristics. Globular mitochondria were identified by their spherical shape, and

elongated mitochondria by a ''capsule'' shape.[30,48,56] The aspect ratio, defined as mitochondrion length divided by width,[30] was also calculated to confirm the morphological categorization. The aspect ratio of globular mitochondria is smaller than elongated mitochondria, and is often a value close to 1.0, given the characteristic spherical shape of globular mitochondria.[30] For each presynaptic mitochondrion, the XY plane with the largest surface area was identified, and the length and width of the mitochondrion (measured from outer membrane to outer membrane) was measured in triplicate. The mean length measurement divided by the mean width measurement generated the aspect ratio.

Each Type 1 axo-spinous synapse was also evaluated for the presence of a spine apparatus or SER in the postsynaptic dendritic spines. Spine apparatuses represent an extension of smooth endoplasmic reticulum (SER) into the spine head and appear as discrete tubular or vesicular structures.[126,127] Annotation as a spine apparatus required a minimum of two cisternae with an electron-dense ''plate'' separating cisternae in at least one ortho-slice when the spine head was evaluated in 3D, and annotation as SER required at least one cisterna with the absence of electron-dense plates.[126,128]

Statistics analyses

All statistical analyses were completed using SPSS software (version 27, IBM, Armonk, NY, USA). Pearson correlation coefficient analyses assessed linear relationships between structure volumes. Chi squared or Fisher's Exact tests determined whether the presence of mitochondria or a spine apparatus differed significantly across synaptic populations. One-way ANOVA tested differences in synaptic compartment and organelle volumes between synaptic populations.